Summer 8-1-2017

Development of the End-Effector of a Cable-Driven Parallel Manipulator for Automated Crop Sensing

Iman Salafian
University of Nebraska - Lincoln, i.salafian@gmail.com

DEVELOPMENT OF THE END-EFFECTOR OF A CABLE-DRIVEN PARALLEL MANIPULATOR FOR AUTOMATED CROP SENSING

by

Iman Salafian

A THESIS

Presented to the Faculty of

The Graduate College at the University of Nebraska

In Partial Fulfillment of Requirements

For the Degree of Master of Science

Major: Mechanical Engineering and Applied Mechanics

Under the Supervision of Professor Benjamin Terry

Lincoln, Nebraska

August, 2017

DEVELOPMENT OF THE END-EFFECTOR OF A CABLE-DRIVEN PARALLEL MANIPULATOR FOR AUTOMATED CROP SENSING

Iman Salafian, M.S.

University of Nebraska, 2017

Advisor: Benjamin S. Terry

A four cable-driven parallel manipulator (4CDPM), consisting of sophisticated spectrometers and imagers, is under development for use in acquiring phenotypic and environmental data over an acre-sized maize field. This thesis presents the design, controls, and testing of two sub-systems in a 4CDPM: a Center of Mass Balance System (CMBS) and a Drop-Down System (DDS).

One of the factors that influences stability is the center of mass (COM) position of the end effector. An offset in COM can cause a pendulum effect or an undesired tilt angle. A center of mass balancing system is presented in this thesis to minimize the vibration and enhance the stability, accuracy, and quality of acquired data from the instruments.

The current design of the 4CDPM enables the sensing of the canopy at normal as well as oblique angles, but the end-effector itself must remain above the canopy; otherwise, the four support cables (and the end-effector itself) may impinge upon the crops surrounding those being imaged. Thus, a supplementary drop-down system is needed for positioning a small sensor package inside the canopy, which enables the researchers to analyze the low-height crops and take images of the side views of the maize canopy.

This thesis is divided into two parts, exploring both devices. Part one focuses on developing a system and method for the CMBS, while part two focuses on the feasibility of the DDS. In each part, the motivation behind each of the devices is described, and the design of the respective device and the reasons behind some of the design choices are presented. Several experiments are designed and executed for both projects, and the results are given for each.

For the CMBS, the results demonstrate that this system improves the stability of the end-effector by decreasing vibrations and static tilt angle. The results for the DDS show that this system needs an additional stabilization system to damp oscillations.

Finally, the conclusion section describes the future work associated with the devices as well as the accomplishments achieved through the design of each device.

ACKNOWLEDGEMENTS

Firstly, I would like to express my sincere gratitude to my advisor Dr. Benjamin Terry for the continuous support of my master's study and related research, for his patience, motivation, and immense knowledge. His guidance helped me the entire time I researched and wrote this thesis. Also, a huge thanks to Dr. Arthur Zygielbaum who provided a lot of guidance in many designs and testing decisions.

Thanks to the other students who worked alongside me in these projects: Blake Stewart and Matthew Newman. Many of the design and testing decisions should be attributed directly to them and the undergraduate students before them who worked on the four cable-driven parallel manipulator project as well. Finally, thanks to my family for their encouragement and support in pursuing a master's degree.

Table of Contents

List of Figures

List of Tables

List of Abbreviations

Abbreviation	**Explanation**
CDPM	Cable-Driven Parallel Manipulator
4CDPM	4 Cable-Driven Parallel Manipulator
CMBS	Center of Mass Balance System
DDS	Drop Down System
FOV	Field of View
COM	Center of Mass

Part I: Center of Mass Balance System (CMBS)

Chapter 1 : An Introduction to Automated Phenotyping Systems

As the population of the world continues to grow, the demand for agricultural productivity will be increased significantly. Also, traditional methods to enhance crop and animal production will face pressures in adapting to population growth [1], [2]. This challenge highlights a need to exploit advanced biotechnology tools to meet increased productivity for both plant and animal systems. Plant phenotyping is one of the methods for identifying plants with desirable traits such as yield, growth, development, tolerance, resistance, architecture, physiology, ecology, etc. Also, plant phenotyping enables researchers to measure quantitative parameters that form the basis for the more complicated traits [3]. The measurement parameters include image-based projected leaf area, chlorophyll fluorescence, stem diameter, plant height/width, crop root characteristics, compactness, stress pigment concentration, tip burn, internode length, color, leaf angle, leaf rolling, leaf elongation, seed number, seed size, tiller number, flowering time, germination time, and so forth [4]–[18].

Remote sensing is one of the methods for precision agriculture and high-throughput phenotyping. Remote sensing is defined as the science of acquiring and analyzing data about an object, an area, or a phenomenon under investigation by a system of sensors that are not in contact with the object, area, or phenomenon under investigation [19]. Remote sensing is a suitable technique for gathering information in a timely manner over large field areas. Remote sensing must be timely because productivity can be affected by unfavorable growing conditions within short time periods [20]. A remote sensing system for precision agriculture includes several sensors, spectrometers, and cameras to collect plant and environmental data. For instance, a hyperspectral imager collects and processes the electromagnetic spectrum of the light reflected and emitted by

the canopy [21]. The collected reflectance data provides a diagnostic tool that may be useful in detecting disease, weeds, and pests; prediction of yield; and crop growth monitoring [22].

Over the years, scientists have explored several remote sensing systems and phenotyping platforms to increase the precision, resolution, and throughput of phenotyping. In traditional remote sensing, operators need to carry field spectroradiometers to the site for collecting the radiometric data (Figure 1-1) [23]. In this method, different hand-held instruments are used or the sensors are mounted on a long pole or yoke to keep them far away from the operator's body (Figure 1-2). The long pole improves the accuracy of the collected data by reducing the amount of reflected light from bright clothing falling on the surface being measured. The data can be transferred from the sensors at the top of the pole to the data logger using optic fibers. The required electronic elements are mounted in a self-contained backpack, which the operator can carry during the experiment [24]. Different supports or fixed frames such as small masts, dedicated towers, and tramways can be used for repeated field spectral measurements [25].

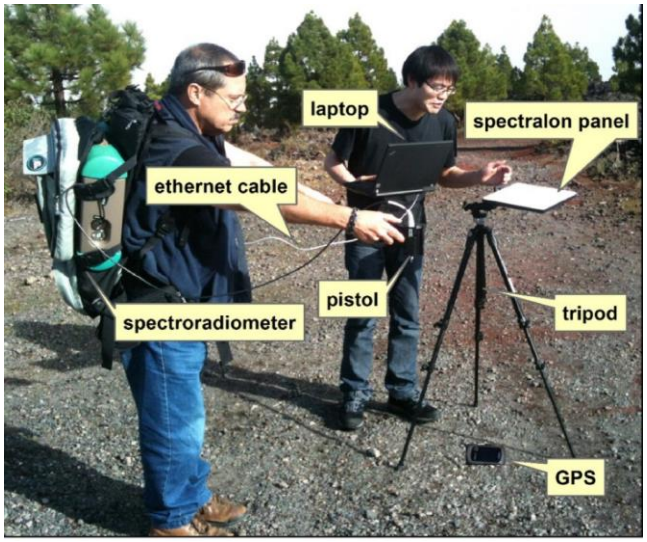

Figure 1-1: Ground-based Remote Sensing for field phenotyping [23]

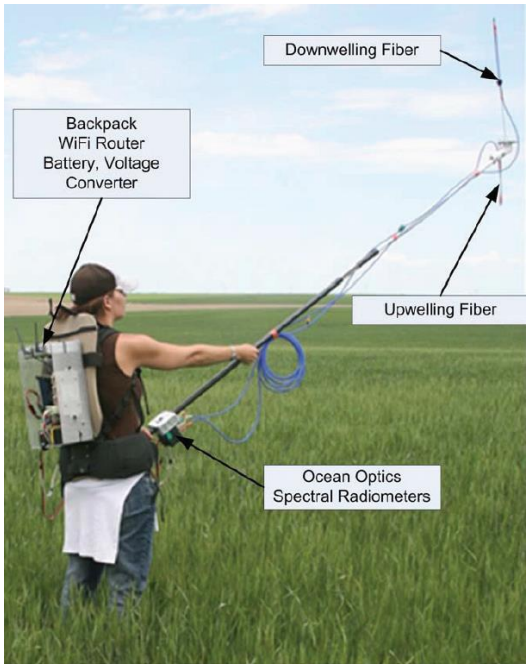

Figure 1-2: Acquiring Spectral-Reflectance Data at Canopy and Plant Community Levels [24]

There are inconsistencies and problems associated with a researcher physically holding and positioning a field radiometer during data collection, such as light reflection, inappropriate weather conditions, and less systematic data collection. Therefore, it is beneficial to have an automated and remotely operated system, which can follow a certain scanning pattern and be far enough from the target to minimize light reflectance from equipment. For instance, the sensor package can be mounted on a variety of motorized booms [26], an all-terrain motorized platform [27], a refurbished tractor [24], or a specially-designed buggy [28]. The aforementioned systems can be automatically operated, and they solve some problems of the handheld platform; however, they are not remotely operated, and the operator still needs to be on site and drive the vehicle. The aerial high-throughput phenotyping platforms (HTPPs), such as unmanned aerial vehicles (UAVs), enable low-cost, rapid data acquisition of the large fields [29]–[32]. However, these systems have a short operation time because they use batteries. UAVs can carry only a small number of sensors, and they are unable to operate in windy weather appropriately. Also, rapid rotation of propellers

produces air turbulence below them that can influence canopy structure. On the other hand, the Field Scanalyzer, which is a robotic field phenotyping platform, can be used to monitor plants automatically, remotely, and permanently [33], [34]. Although this platform incorporates a motorized overhead gantry for precisely carrying a heavy sensor package, it casts shadows on the crops and reflects sunlight to the canopy, which can skew the radiometric data [35]–[37]. To overcome the problems mentioned above, a system must be designed that can operate automatically, and remotely with high precision and flexibility during a predetermined schedule in different weather conditions. This system must be able to work with minimal interference in canopy structure without casting a shadow or reflecting light on the canopy. In the next chapter, cable robots are introduced as the potential systems for the remote sensing of large fields with an ability to carry a high payload of sensors with minimal shadow and interference in acquiring phenotyping data.

Chapter 2 : An introduction to the four cable-driven parallel manipulator

Serial robots are the most common industrial robots successfully performing in numerous industrial processes such as handling, machine assembly, and welding. They are designed as a series of links connected by motor-actuated joints that extend from a base to an end-effector [38], [39]. In robotics, an end effector is the device at the end of a robotic arm, designed to interact with the environment. The exact nature of this device depends on the application of the robot [40]. The serial robots, however, are limited in their payload and workspace, which is a significant issue for the remote sensing systems, since the sensor package in a remote sensing system includes several heavy sensors that have to scan a large field. On the other hand, parallel manipulators use several computer-controlled serial chains to support a single end-effector [41]. One of the well-known parallel robots with large workspace is the so-called "cable driven parallel manipulator (CDPM)."

Cable-driven parallel manipulators (known as cable-suspended robots or wire-driven robots) are a type of parallel manipulator in which flexible cables are used as actuators. One end of each cable is reeled around a rotor twisted by a motor, and the other end is connected to the end-effector [42]. CDPMs can cover wide workspaces, and their payload to weight ratio is usually very high. Their price varies depending on the size of the system, but they are relatively cheap in small sizes and can be designed in such a way to be reconfigurable and therefore adaptable to different tasks [43]. One famous example of cable robots is the Spidercam [44], which is used to move a suspended camera in stadiums. The first cable-driven robots were designed and developed as early as 1989. The RoboCrane system at NIST was one of the first prototypes for large scale handling [45], [46]. Later in 1999, a cable robot was designed for fast pick-and-place jobs [47], and a mobile cable robot system was developed for rescue after earthquakes [48]. In the 21st century, more

research was done on cable-driven robots, and their applications were broadened in several different areas. For instance, a light weight structure with a six-degrees-of-freedom cable robot was used for motion generation in wind tunnels [49]. In 2004, a research team at the University of Rostock, Germany, developed their tendon-based parallel manipulator with a parallel kinematic structure—i.e. the Stewart–Gough platform. The purpose of this work was the analysis of workspace singularities, forward kinematics, and trajectory planning in this type of manipulator [50]–[52]. Further developments and achievements in this area encouraged more scientists to use cable robots in their research. This interest led to the design and development of the robot String-Man, which was used at Fraunhofer IPK (Berlin, Germany) for gait-rehabilitation with a focus on force control and safety considerations [53], [54]. In 2009, a research group in Canada developed a parallel cable-driven haptic interface and analyzed computational methods for addressing the issues regarding human safety and control reliability using such an interface [55], [56]. In 2015, Fraunhofer IPA developed an eight-cable parallel robot for studying motion perception with possible applications in neurological research into balance disorders. A large workspace and dynamic capabilities made the simulator suitable for a broad spectrum of virtual reality applications, including driving/flight simulation as well as investigation of basic perception processes in humans [57].

Our platform is based on the successes achieved with the Five-hundred-meter Aperture Spherical radio Telescope (FAST) project [58]–[61] and the Field Phenotyping Platform (FIP) [62], [63]. The FAST is the world's largest filled-aperture radio telescope with a fixed 500 m diameter dish constructed in a natural depression. The end effector of the FAST is moved around the workspace using a six-cable driven system. The FIP is an eight-cable driven parallel manipulator (8CDPM) for automated, image-based crop phenotyping, which is designed and built

by the Spidercam Company (Figure 2-1) [62]. The FIP uses four winches that are positioned in each corner of the field near each pole. Two catenary cables are uncoiled from each winch to two pulleys that are mounted at the top of each pole in sufficient height (Figure 2-2). Pulleys constitute the points of suspension for the catenary cables carrying a dolly (Figure 2-3). The dolly carries the sensors using the pan-tilt unit (PTU). The PTU is able to turn the sensors in two axes, pan and tilt.

The winches are interconnected via fiber optics with a control unit. The control unit features an industrial PC, a control desk, and a computerized safety device. The computer program installed in the industrial PC processes all data and on the basis of the achieved results, and calculates the required rotary motion of each winch. Joysticks embedded in the operation desks serve to effectuate the desired movements of the dolly.

Figure 2-1: Overview of the ETH Field Phenotyping Platform (FIP) [62]

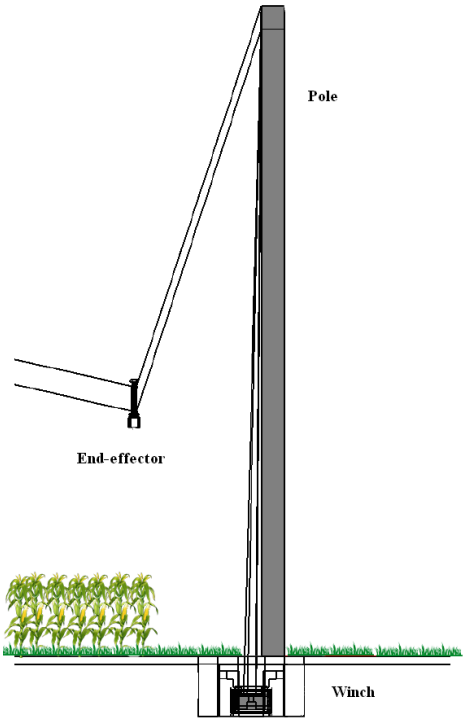

Figure 2-2: A schematic of pole, winch, and end-effector in the FIP

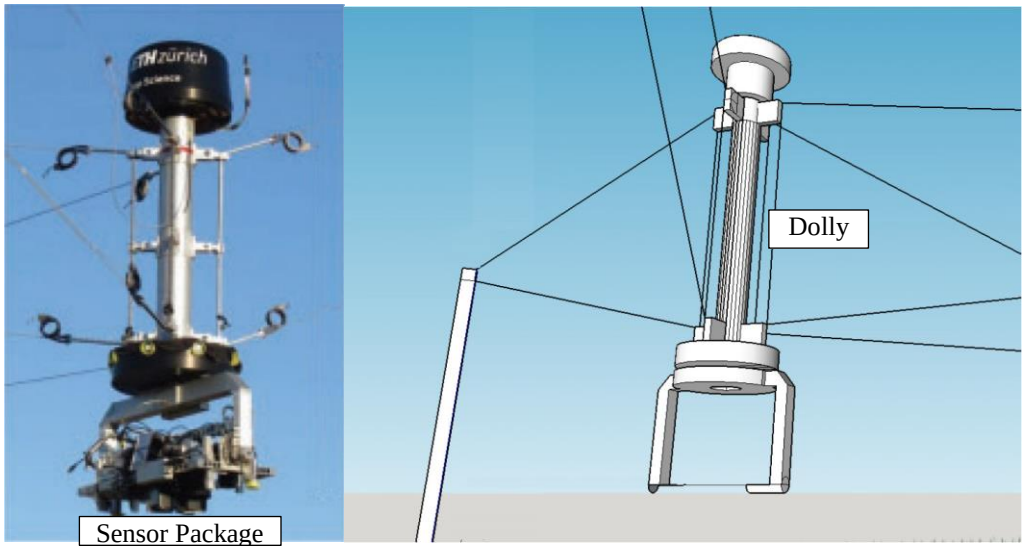

Figure 2-3: Sensor head of FIP carried by eight cables

Even though the FIP is known as one of the best phenotyping systems [64], it still has some limitations. Mounting with eight cables makes the sensor head resistant to tilt motion due to the wind or other disturbances, but there is a high amount of induced tilt when the end-effector is moved to the edges of the field. The reason is that tension in one or two of the cables is higher than the other cables causing the end-effector to incline. To compensate for this tilt, poles need to be positioned outside of the working area. This ensures that the forces applied to the end-effector stay low enough to avoid influencing the upright position of the platform. The minimum distance from the outer border of the working area is directly related to the distance between the pulleys. According to the Spidercam report, the distance from the poles to the working area should be no less than 7% of the length of the working area. As this applies to both directions, the distance between the poles is 14% bigger than the working area. Another method for decreasing the induced tilts is using actuators or a gimbal system. However, actuators add to the size, cost, weight, and complexity of the system and the motion of the gimbal system must be controlled precisely to avoid causing a pendulum effect or orientation change.

It is well known that an end-effector in a CDPM can be positioned in space using only three poles, winches, and cables (Figure 2-4a). However, three systems of cables and winches are useful to cover a triangle workspace. In order to have a square workspace the poles need to be located very far from each other (Figure 2-4b). A system of four poles and four cables can be used to decrease the pole area in the same size workspace (Figure 2-4c). The FIP uses four poles but **eight** cables to position the end-effector in a square workspace. The four additional cables constrain the end-effector in space and create a relatively rigid support for the end-effector, which prevent the end-effector from pendulum effect. However, the four additional cables increase

redundancy, complexity and the total cost of the system since the end-effector can be suspended only from four cables to scan a square field.

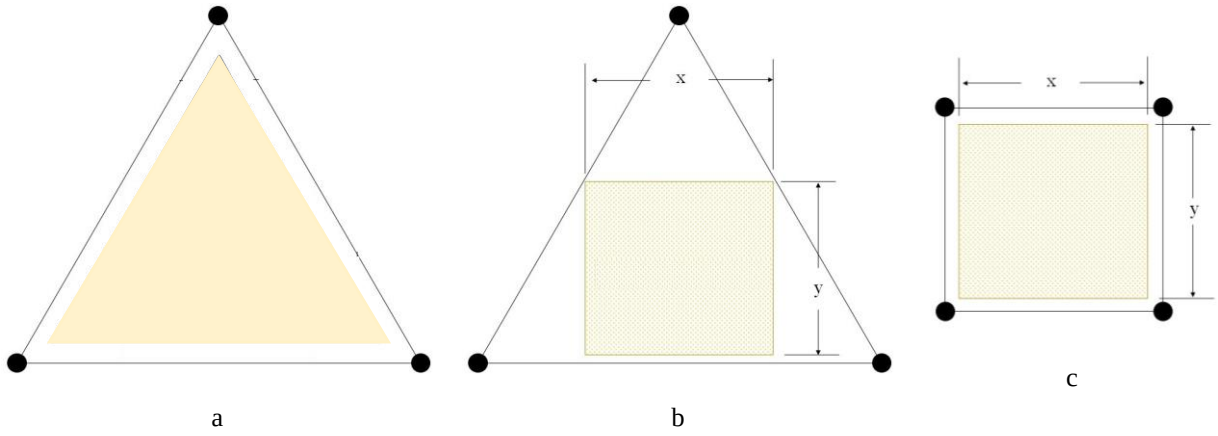

Figure 2-4: Potential cable system layouts. a) Three pole system with a triangle workspace. b) Three pole system with a square workspace. c) Four pole system with square workspace.

Also, the FIP lacks the fine-tuned, active stabilization to compensate for disturbances. For instance, long cables can experience a high amount of catenary, which makes the end-effector less rigid and difficult to control during windy weather.

The four-cable driven phenotyping parallel manipulator (4CDPM), on the other hand, is an optimized cable driven phenotyping robot proposed by the principal researchers at the University of Nebraska-Lincoln. The purpose of this system is to scan a one-acre maize field at Mead, Nebraska. The field contains multiple plots arranged in a grid, and the 4CDPM will be programmed to visit the plots to acquire phenotypic and environmental data based on a predetermined schedule (Figure 2-5).

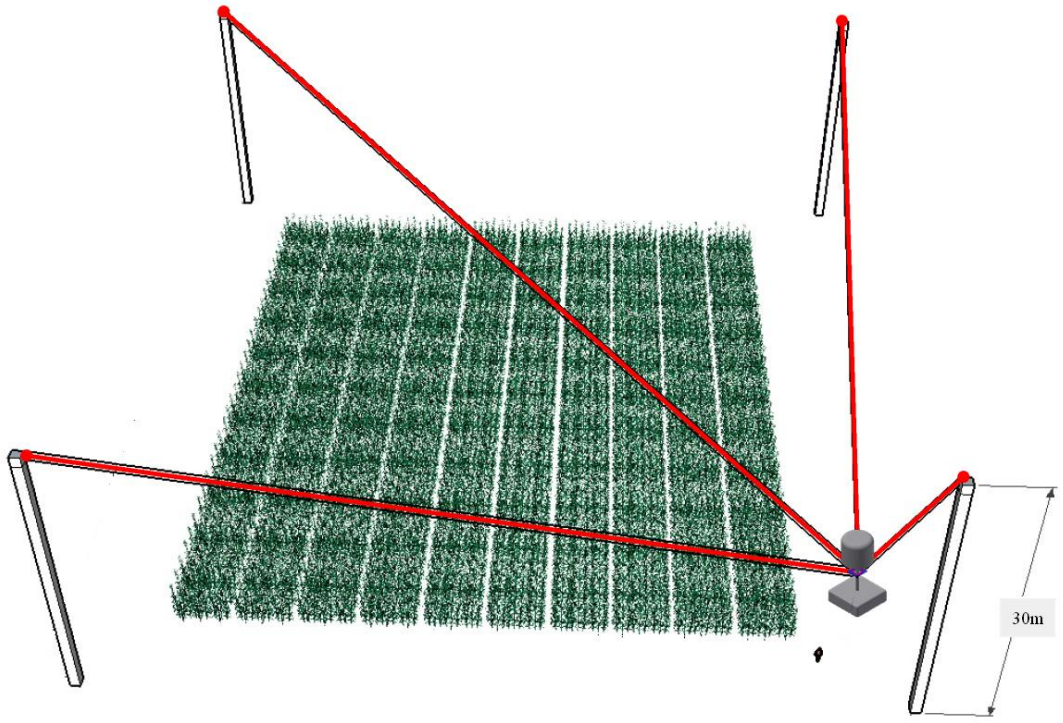

Figure 2-5: The field containing multiple plots arranged in a grid

The system must be able to provide precise positioning of the sensor package around the field and operate smoothly without significant vibration at 30 mph (13.4 m/s) wind speed. The system needs to work automatically based on the predetermined schedule and carry a sensor package with a maximum weight of 30 kg without casting a significant shadow or reflecting light on the crops. As shown in Figure 2-6, the 4CDPM uses only four pulleys and winches to position the sensor package over the field, reducing the complexity and the cost of the system and preventing the end-effector from tilting at the edges of the field using a gimbal system. An active stabilization system contributes to vibration damping and maintains the sensor package in a stationary position for high-quality imaging.

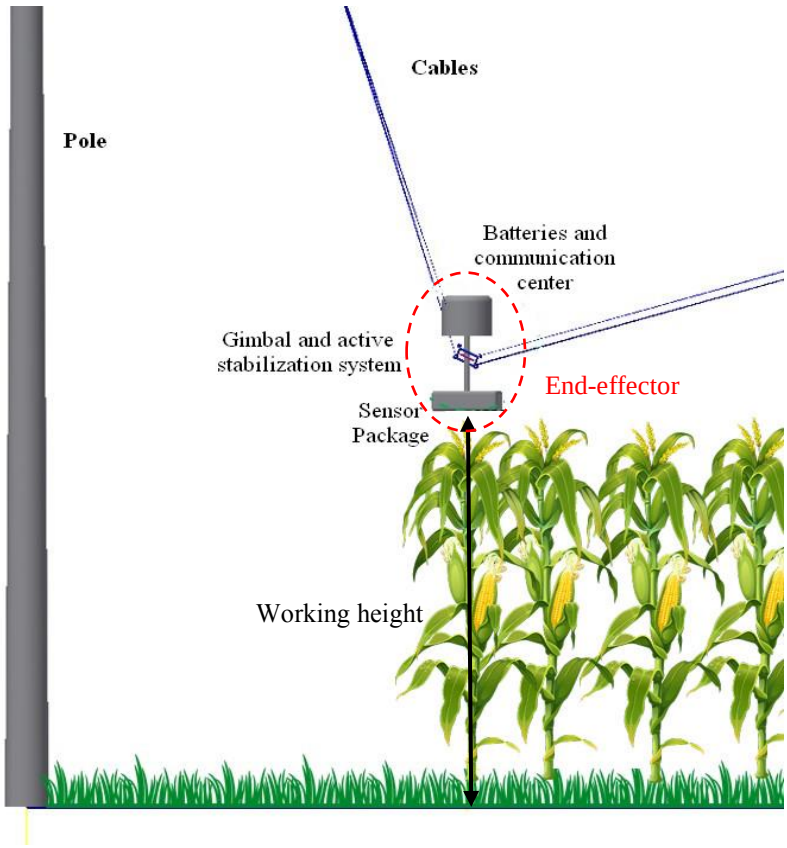

Figure 2-6: Four cable-driven parallel manipulator

Table 2-1 shows the main desired design specifications of this system, which were determined by researchers at the University of Nebraska-Lincoln. The pole's height was selected according to the working area, maximum allowable tension in the cables, and working height. Using shorter poles requires the system to use stronger cables while taller poles need a deeper foundation and more material, which increases the cost of the system. Also, tall poles are susceptible to deflection and vibration in windy weather or when the cables are under high tension. An adequate limit for acceleration and speed ensures that the sensor package scans the field in the scheduled time line. The accuracy of the end-effector's position in the field was defined by the rotation and translation accuracy values. Sufficient accuracy ensures that the sensor package is close enough to the targeted plane. The required dynamic stability of the end-effector also needs to be defined which is used in the design of the stabilization system. Since each sensor has a

specific integration time and shuttle speed, it is important to maintain the sensor package stable enough to prevent blurry images. However, further studies must be carried out for determining the dynamic stability accuracy of the sensor package. Thus, Chapter 3 discusses the effect of the end-effector oscillation on the captured images. Also, in this chapter, the dynamic stability accuracy of the sensor package is obtained.

Table 2-1: Main design specifications of 4CDPM

Working area	60 x 67m
Pole height	30m
Working height	0.5 – 10m
Maximum Speed	2m/s
Maximum acceleration	1m/s^2
Maximum payload	130 kg
Rotation Accuracy	+/- 5 degrees
Vertical Translation Accuracy	20 cm
Horizontal Translation Accuracy	20 cm
Maximum Wind speed	30 mph (13.4 m/s)
Dynamic Stability in Rotation	Unknown
Dynamic Stability in Translation	Unknown

As discussed above, a gimbal system is used in the 4CDPM to maintain the end-effector vertical or the sensor package in a nadir position for scanning the canopy efficiently. One of the important factors in the stability of a gimbal equipped end-effector is the location of the center of mass (COM). Gimbal systems are sensitive to COM positions that are not in line with the point of

motion. Any offset in the COM of the end-effector from its point of motion can cause an external moment and tilt in the end-effector, consequently changing the orientation of the sensor package or causing a pendulum effect. Therefore, in Chapter 4, a center of mass balancing system (CMBS) is developed to minimize the vibration and enhance the stability, accuracy, and quality of acquired data from the instruments.

Finally, in Chapters 5 to 8, a supplementary system is developed for optimizing the end-effector functionality by positioning a small dolly inside the canopy. This system enables the researchers to analyze low-height crops and take images of the side views of the plants.

Chapter 3 : The effect of end-effector oscillation on the captured images

One of the most important factors for getting good data in the plant remote sensing is taking images with high spatial, spectral, temporal, and radiometric resolutions without significant blur and smear [65]. When a camera creates an image, that image may not represent a single instant of time. Because of technological constraints, the image may represent the scene over a period of time. Most often, this exposure time is brief enough that the image captured by the camera appears to capture an instantaneous moment, but this is not always so, and a fast moving object or a longer exposure time may result in blurring artifacts, which make this apparent. As objects in a scene move, an image of that scene must represent an integration of all positions of those objects, as well as the camera's viewpoint, over the period of exposure determined by the shutter speed. In such an image, any object moving with respect to the camera will look blurred or smeared along the direction of relative motion [66].

It is difficult to obtain a clear image in the end-effector of 4CDPM since the sensor package is suspended from the flexible cables and undergoes different sources of vibration. In addition, the cameras and spectrometers in the proposed 4CDPM have an integration time ranging from 2 ms to 33 ms (Table 3-1). The long integration time in the high resolution spectrometer requires the sensor package to stay relatively motionless above the canopy. Since it is not technically possible to keep the sensor package motionless, it is essential to know the allowable vibration amplitude and speed of the end-effector in different directions during the data collection.

Table 3-1: List of sensors with imaging integration time information

Sensor name	Speed	Integration time
Hyperspec® Inspector	100-450 Hz	2ms - 10 ms
IR Camera	50 - 200 Hz	5ms - 20ms
VNIR Camera	30 Hz	33 ms

Figure 3-1 shows the three main oscillation directions of a camera . When the end-effector is at a specific height above the canopy, a very small change in the position or orientation can cause a considerable error in the captured image of the canopy. Figure 3-2 and Figure 3-3 show the effects of vertical oscillation of the camera on the captured image compared to a clear image of the canopy from a stationary position of the camera.

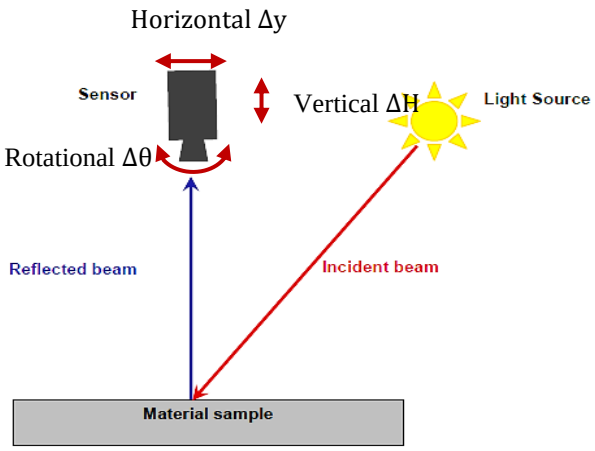

Figure 3-1: Movement of camera above the canopy in different directions

Figure 3-2: A clear image of canopy in stationary position of camera

Figure 3-3: The effect of vertical oscillation of captured image

The image in Figure 3-3 has a considerable blur in comparison with Figure 3-2 because the camera had a substantial position change during the exposure time of the camera.

With the above considerations in mind then, two important questions must be answered. First, how much motion blur in the captured image is allowable to result in scientifically acceptable spectral data? Second, how much oscillation amplitude and vibration speed are allowed for taking an image with sufficient clarity?

The principal investigators at the University of Nebraska-Lincoln suggested the total motion blur of 1% due to all modes of motion. It means that the size change in the target object must not exceed 1% of the image size. However, this number is a rough estimation for simplifying the future calculations and may be changed if a higher or lower clarity is needed. Figure 3-4 shows a simple schematic, which demonstrates the effect of various modes of motion on a image taken from a leaf. This figure indicates that the rotational and horizontal movements cause a small offset in the final image, while the vertical movements shrink or enlarge the image. According to the definition mentioned above, the amount of shrinkage or enlargement of the image must not exceed 1% of the size of the image.

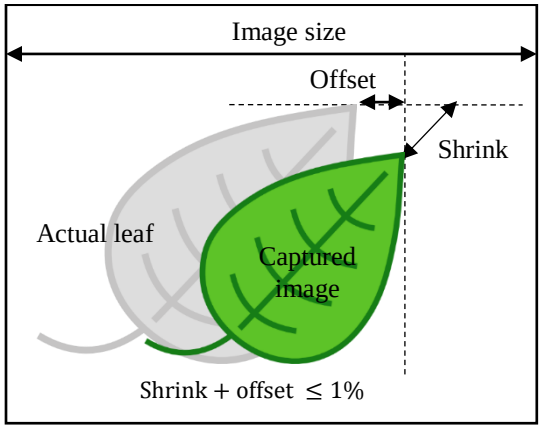

Figure 3-4: Schematic demonstration of errors in taking image

In the next section, an analytical study is carried out on each mode of vibration. Also, a set of equations is obtained, which correlates the maximum motion blur to the maximum allowable oscillation amplitude and vibration speed.

3.1 Induced motion blur due to vertical motion

To begin with, the effect of the changing height on the captured image needs to be determined. Figure 3-5 shows a square, which is drawn on letter-size paper. The camera is placed above the paper and two images are taken from the square ahead of paper at two different heights (10 cm and 15 cm). The length of square side when the camera is located at 10 cm and 15 cm above the paper are d_1 and d_2 respectively. The field of view (FOV) of this camera is constant, which results in the same image size of 960 by 1280 pixels in both images. The square size is smaller in the second image where the camera is located at the higher altitude while the overall size of the image is still 960 by 1280 pixels (Figure 3-5b).

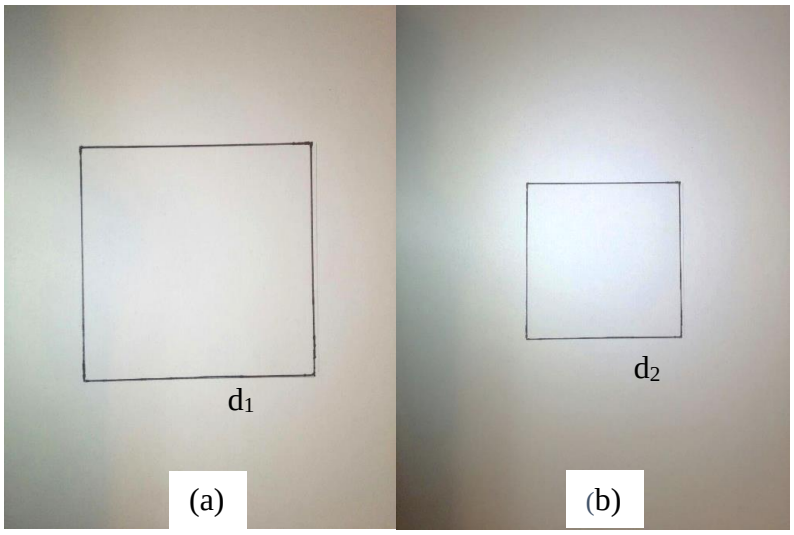

Figure 3-5: The effect of the change in elevation on the dimensions of a captured targethe ground.

In Figure 3-6, shrinking of the image is imaged schematically, where the change in height is ΔH and the expansion of the target area is shown by Δx. Each sensor has a particular field of view that is represented by θ. According to Figure 3-6, when the height of the camera (ΔH) changes, the viewed area increases or decreases by Δx. The relation between ΔH and Δx is

$$\Delta x + x_1 = (H_1 + \Delta H) \times \tan\frac{\theta}{2} \tag{3-1}$$

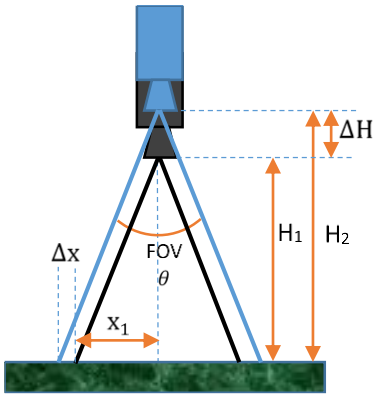

Figure 3-6: Shrinking the image due to increasing elevation.

It is apparent that when the height of the camera increases, the viewed area increases as well; however, objects in the first image (with low height camera) are shrunk or scaled down in the second image (higher altitude camera) to accommodate the constant image size. Therefore $\Delta x + x_1$ in the second image must be shrunk to its first amount, Δx. For instance, in Figure 3-5, the square side in the first image is d_1 but it is reduced to d_2 after increasing the height. The amount of shrinkage (d_1-d_2) can be found using the following equation:

$$\frac{\text{The length of target in 2nd image}}{\text{The target's length in the 2nd image shrunk to the amount of the 1st image}} = \frac{\text{The length of square side in the 1st Image}}{\text{The length of shrunk square side in the 2nd image}} \tag{3-2}$$

It can be written in the analytical form:

$$\frac{\Delta x + x_1}{x_1} = \frac{d1}{d2} \Rightarrow d2 = d1 \times \frac{x_1}{\Delta x + x_1} \tag{3-3}$$

Subtracting both sides from d1:

$$d1 - d2 = d1 - d1 \times \frac{x_1}{\Delta x + x_1} = d1 \times \left(1 - \frac{x_1}{\Delta x + x_1}\right) \Rightarrow \Delta d = d1 \times \frac{\Delta x}{\Delta x + x_1} \quad (3\text{-}4)$$

Consequently, the amount of motion blur would be:

$$\text{Motion blur in vertical motion} = \frac{\Delta d}{d1} = \frac{\Delta x}{\Delta x + x_1} \quad (3\text{-}5)$$

It is more convenient to rewrite this equation as a function of H. According to (1) and

$$x_1 = H_1 \times \tan\frac{\theta}{2} \quad (3\text{-}6)$$

the motion blur would be:

$$\text{Motion blur in vertical motion} = \frac{\Delta d}{d1} = \frac{\Delta H}{\Delta H + H_1} \quad (3\text{-}7)$$

3.2 Induced blur due to rotational motion

Motion blur in the captured image can also happen when the sensor slightly rotates as shown in Figure 3-7. Assuming x_1 as the length of camera's target area, and θ as the field of view of the camera, the governing relation for calculating the amount of blur due to change in the sensor's angle can be found using a similar approach.

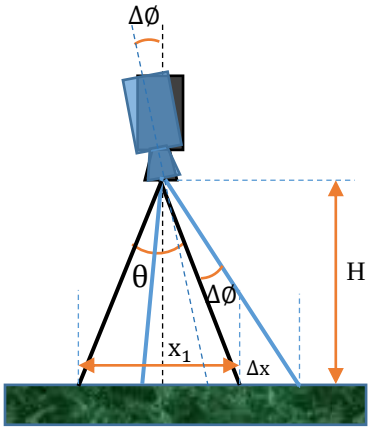

Figure 3-7: Error due to the rotational movement of sensor

Since

$$x_1 = 2H\tan\left(\theta/2\right) \tag{3-8}$$

and

$$x_1 + \Delta x = H\tan\left(\theta/2\right) + H\tan\left(\theta/2 + \emptyset\right) \tag{3-9}$$

Assuming $\theta \neq 0$, and $\Delta\emptyset$ very small, the blur in the rotation is:

$$\begin{aligned}\text{Motion blur in rotation} &= \frac{\Delta x}{x_1} = \frac{H\tan\left(\theta/2\right) + H\tan\left(\theta/2 + \Delta\emptyset\right) - 2H\tan\left(\theta/2\right)}{2H\tan\left(\theta/2\right)} \\ &= \frac{\tan\left(\theta/2 + \Delta\emptyset\right) - \tan\left(\theta/2\right)}{2\tan\left(\theta/2\right)}\end{aligned} \tag{3-10}$$

3.3 Induced motion blur due to horizontal motion

Finally, the motion blur due to the horizontal movement is shown in Figure 3-8

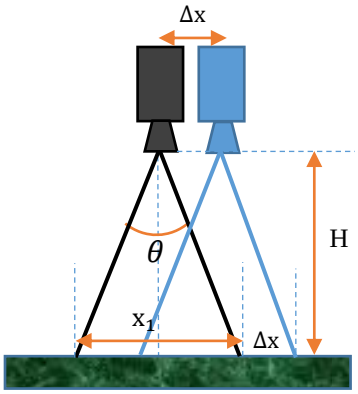

Figure 3-8: The error due to horizontal movement

The equation can be derived from Figure 3-8, which is a change in motion divided by x_1.

$$\text{Motion blur in horizontal motion} = \frac{\Delta x}{x_1} = \frac{\Delta x}{2H\tan(\theta)} \tag{3-11}$$

3.4 Maximum allowable amplitude of motion

As mentioned before, the total motion blur in the image taken by the imager due to the movement of the sensor in all directions must be less than 1%:

$$\text{Horizontal} + \text{Rotational} + \text{Vertical} \leq 1\%$$

It is important to know the impact portion of each motion in the total 1% allowable motion blur. All of the relations above for calculating motion blur were initiated from a fundamental definition of $\frac{\Delta x}{x_1}$. Therefore the following relation is generally true:

$$\frac{\Delta x}{x_1} + \frac{\Delta x}{x_1} + \frac{\Delta x}{x_1} \leq 1\% \Rightarrow \frac{\Delta x}{x_1} \leq \frac{1}{3} \times 1\% \tag{3-12}$$

It can be concluded that mode of blur needs to be less than $0.\bar{3}\%$. Thus

$$\text{Blur in Rotation} = \frac{\tan\left(\theta/2 + \Delta\emptyset\right) - \tan\left(\theta/2\right)}{2\tan\left(\theta/2\right)} \leq \frac{1}{3} \times \frac{1}{100} \tag{3-13}$$

$$\text{Blur in vertical motion} = \frac{\Delta H}{\Delta H + H_1} \leq \frac{1}{3} \times \frac{1}{100} \tag{3-14}$$

$$\text{Blur in horizontal motion} = \frac{\Delta x}{2H\tan(\theta)} \leq \frac{1}{3} \times \frac{1}{100} \tag{3-15}$$

After solving the above equations for $\Delta H, \Delta\emptyset$ and Δx, it can be seen that ΔH is only a function of height (H) and Δx is a function of height (H) and θ. Angle change $\Delta\emptyset$ is only a function of θ, which is assumed 30° (it is the field of view for hyperspectral imager [67]) in this study. Therefore, $\Delta\emptyset$ is calculated 0.095°, which does not change with height change. That means that the end-effector at any operating height should not have a rotational vibration more than 0.095 degrees. Figure 3-9 and Figure 3-10 show the diagram of ΔH and Δx versus height for the vertical and horizontal motion respectively. The interval of the height for the operation of the end-effector was defined between 0.5 m and 10 m according to the design features of the 4CDPM. However, when the plant is in full growth, the minimum operation height will be 5 m. Therefore on both figures, the maximum allowable motion is shown for the important heights.

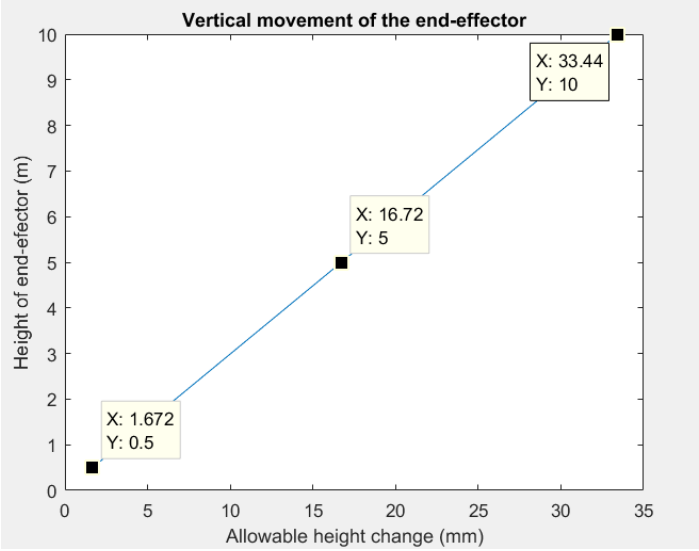

Figure 3-9: Allowable height change (mm) at different heights of the end-effector

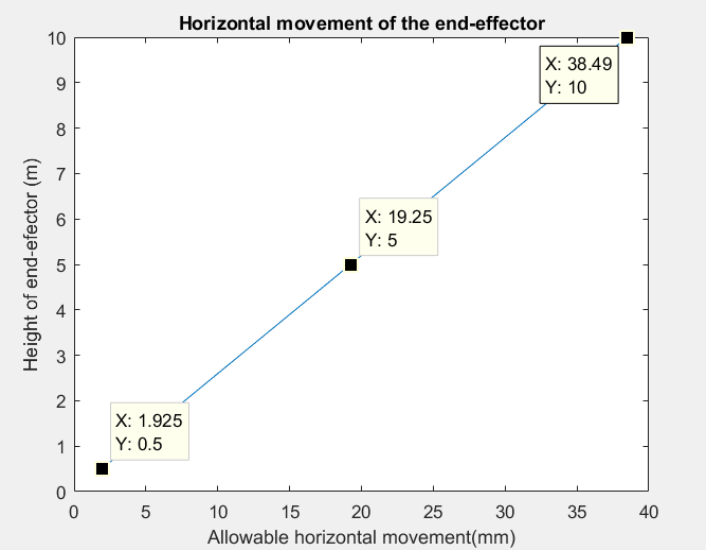

Figure 3-10: Allowable horizontal vibration amplitude in various height of the end-effector

It can be seen in Figure 3-9 and Figure 3-10 that the minimum amount of the maximum allowable horizontal and vertical motion happens when the end-effector is at the lowest height (0.5 m) above the canopy. It means that the height 0.5 m is the most important point as a reference for designing the stabilization system. For example, the stabilization system needs to damp and keep the horizontal oscillations less than 1.925 mm where the end-effector is at 50cm above the ground.

3.5 Maximum vibration speed

In the current sensor package, three important spectral cameras must be located in a sealed and waterproof housing: a hyperspectral spectrometer, a visible and near-infrared (VNIR) camera, and an infrared (IR) camera [68]–[71]. Some of the sensors must be perpendicular to the canopy, and others have to sense crops both nadir or with a particular angle. Each sensor has a particular integration time, which was listed in Table 3-1. For instance, the hyperspectral spectrometer needs at most 10 ms to take the image with the best resolution, and the VNIR camera needs at most 33 ms to integrate all the input data. The integration time is a major factor in designing the stabilization system because, in the interval of time that the sensor is taking images, any position change of the camera will cause a blur and skew the results. For instance, the VNIR camera, which has the longest exposure time, is more sensitive to motion than the other sensors.

Therefore, both time and magnitude of movement are important factors in defining stabilization specification. According to the aforementioned definition for motion blur and considering the integration time, the maximum blur of the captured image in the high resolution spectrometer in 10s must be less than 1%. This definition indicates the importance of velocity in designing the stabilization system. Therefore, using the equations (3-13) to (3-15) and dividing ΔH, $\Delta\theta$, and Δx by time, the velocity equations can be obtained.

$$\Delta H = \frac{bH_1}{3-b} \Rightarrow V_v = \frac{bH_1}{(3-b)t} \tag{3-16}$$

$$\Delta\emptyset = \tan^{-1}\left(\frac{2b}{3}\tan\left(\frac{\theta}{2}\right) + \tan\left(\frac{\theta}{2}\right)\right) - \frac{\theta}{2} \Rightarrow V_\theta = \frac{\tan^{-1}\left(\frac{2b}{3}\tan\left(\frac{\theta}{2}\right) + \tan\left(\frac{\theta}{2}\right)\right) - \frac{\theta}{2}}{t} \tag{3-17}$$

$$\Delta x = \frac{2}{3}bH\tan(\theta) \Rightarrow V_h = \frac{2bH\tan(\theta)}{3t} \tag{3-18}$$

where b is the blur (defined 1%), V_v is the vertical speed, V_θ is the rotational speed, and V_h is the horizontal speed of the camera. For instance, considering the time of moving equal to the

integration time of 33 ms, the diagrams of the maximum allowable velocity of the end-effector in each direction versus height are plotted in Figure 3-11 and Figure 3-12. In the rotational motion, since $\Delta\emptyset$ was caculated 0.095°, the maximum angular velocity is $\frac{\Delta\emptyset}{t} = 2.8\ \frac{deg}{min}$ not changing with height.

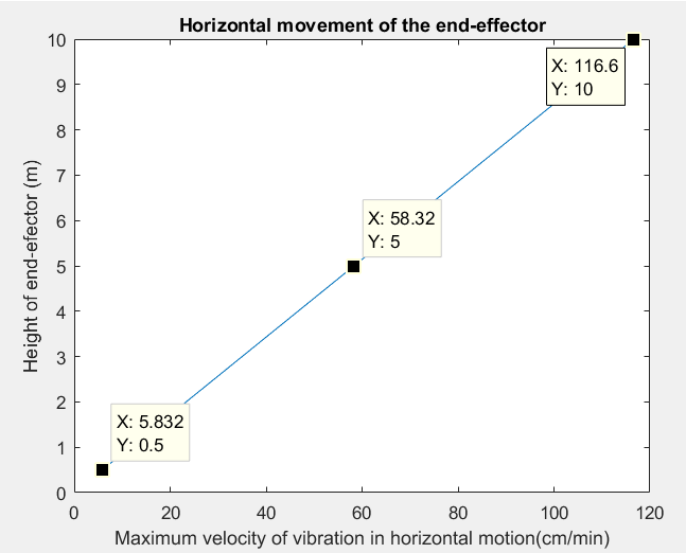

Figure 3-11: Maximum velocity of vibration in the vertical motion (cm/min)

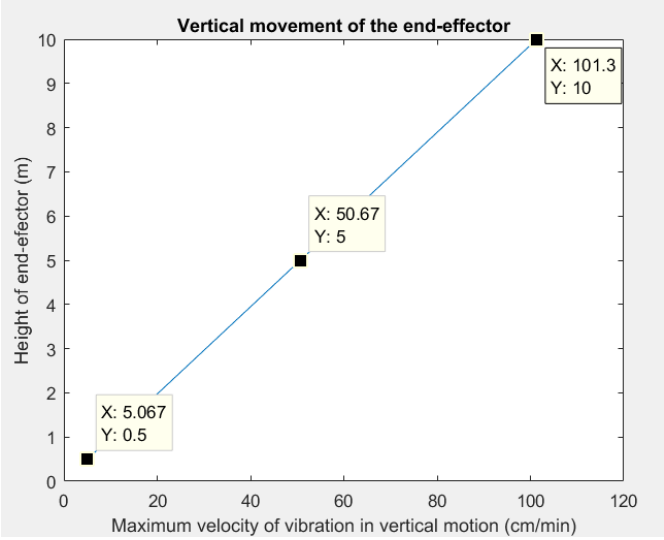

Figure 3-12: Maximum velocity of vibration in the horizontal motion (cm/min)

With the same hypothesis for the maximum allowable movement in each direction, the most sensitive point for designing the stabilization system is at 0.5 m above the ground. The

maximum allowable velocity of the vertical, rotational, and horizontal motion at this point are 5.8 cm/min, 2.8 deg/min, and 5 cm/min respectively.

3.6 Conclusion

In this chapter, first, the effect of the end-effector's vibration on the captured image of the camera was studied, and the relations between the end-effector's vibration and the motion blur in the image were derived. The result showed that the maximum allowable horizontal and vertical movement happened when the end-effector was at the lowest height (0.5 m) above the canopy. It means that the height, 0.5 m, is the reference point for designing the stabilization system.

Next, the motions' error relations were developed to address the problem of long integration time in the cameras for taking the images. Then, the velocity equations were obtained, and the results of the maximum allowable vibration velocity based on using high resolution spectrometer were plotted. The results showed that the critical point is 0.5 m above the ground. In this spot, the high resolution spectrometer needed to have a lower speed of vibration than the rest of the cameras. It means that the vertical, rotational, and horizontal speed of motion in the stabilization system must be below 5.8 cm/min, 2.8 deg/min, and 5 cm/min respectively in order to meet the design constraints of the maximum motion blur of 1%.

The results of this section are used in the following chapters for evaluating the functionality of the designed systems.

Chapter 4 : Center of Mass Balance System (CMBS)

As mentioned in Chapter 2, a four cable-driven parallel manipulator (4CDPM), consisting of sophisticated spectrometers and imagers, is under development for use in acquiring phenotypic and environmental data over an acre-sized crop field. The location and orientation of the 4CDPM sensor package must be precisely controlled and known so that position-sensitive data can be acquired. For example, to compute accurate plant morphology, the location and orientation of the sensor package of the 4CDPM relative to the plant must be known.

Several factors make it difficult to determine the location of the dolly accurately. For example, the wind drag force creates a disturbance to the 4CDPM poles, catenary cables, and the dolly itself causing gross positioning error as well as vibration. Also, inertial forces from the acceleration of the dolly as it moves from plot to plot contribute to vibration in the entire 4CDPM system. As currently designed, the positioning control of the 4CDPM is based on closed-loop control of the winches. The feedback sensor for this control system is the rotary encoder on the winch itself. Thus, the reported position of the dolly contains an error, which is caused by the aforementioned disturbances.

To obtain accurate and high-quality data from the instruments, the end-effector must be stable during sensing. The current 4CDPM uses a gimbal system to maintain the end-effector always vertical above the canopy. One of the important factors in the stability of a gimbal-equipped end-effector in a 4CDPM is the location of the center of mass (COM). Gimbal systems are sensitive to the COM position that is not in line with the point of motion. Any offset in the COM of the end-

effector from its point of motion can cause an external moment and tilt the end-effector, consequently changing the orientation of the sensor package or causing a pendulum effect.

As shown in Figure 4-1a, while the center of force (indicated by F) passes through the COM, the dolly will translate, but will not rotate. However, if the COM does not lie on the center of the force vector as shown in Figure 4-1b, the inertial force from the mass of the dolly and the applied force will form a force couple, which induces a torque on the dolly, causing it to rotate as well as translate. The rotation is an additional dynamic disturbance that induces vibration and reduces the accuracy of imaging. This condition is mitigated by low start and stop acceleration as the dolly moves from plot to plot, or waiting for the vibration to die out once the dolly has reached its destination. Both of these solutions are undesirable because they add time between plot scans. The modular nature of the present design of the dolly contributes to this form of rotational instability because sensors can be added and removed, thus altering the center of mass. Presently, this problem is mitigated by using weights in the place of removed sensors. However, this is not a sustainable solution because the sensing technology changes rapidly, typically resulting in lighter, smaller sensors. Thus, to maintain rotational stability, the dolly hardware must be continually modified in tandem with sensor changes—an undesirable situation in the long-term.

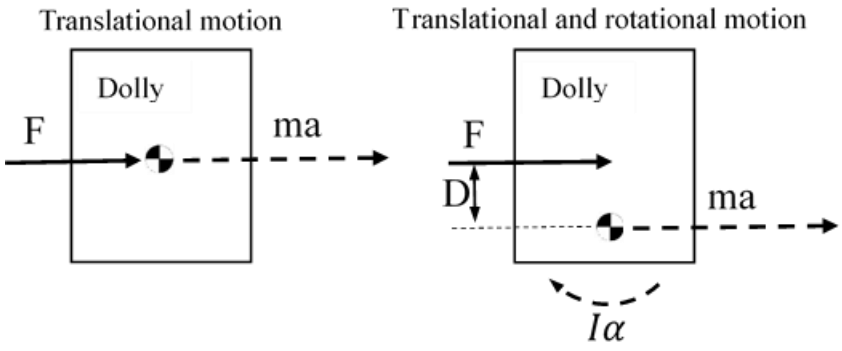

Figure 4-1: Schematic showing the center of force, F

The purpose of this chapter is to develop a system and method for balancing the COM. Also, in this chapter, a proof of concept prototype is designed, built and tested in the 4CDPM end-effector. This device enables the operator to reposition the end-effector's COM easily and quickly in response to the arbitrary changes made to the sensor suite. A 12^{th}-scale 4CDPM is built to validate the concept and test its performance.

In section 4.1, first, the concept and mechanical design of the CMBS is discussed, and the governing statics equations are described. Next, the important components including an electronic circuit board for collecting orientation data are presented. Also, in this section, the design features and characteristics of the 12th-scale 4CDPM are introduced. Section 4.2 discusses the details of the experimental procedure for proving the functionality of the device and shows the collected data from sensors. Section 4.3 examines the results of the experiments and explains the improvements in the system after using the CMBS. Finally, section 4.4 offers some concluding remarks and explains a summary of achievements, which are accomplished in this research.

4.1 Materials and methods

The complete four cable-driven phenotyping platform includes poles, winches, cables and the end-effector. The end-effector contains a sensor package, a dolly for mounting the sensor package, gimbal system, and an active or a passive stabilization system (see Figure 2-2, Figure 2-3, and Figure 2-6). To achieve scientifically accepted phenotyping results, each part should be accurately designed and built. In this section, the design features and functional abilities of the important parts are explored in a 12^{th}-scale system. Also, a CMBS is introduced, which serves as the passive stabilization system in the 12^{th}-scale 4CDPM.

4.1.1 Center of mass balance end-effector

The Center of Mass Balance System (CMBS) consists of five main components, which are assembled by pins and screws: a vertical acrylic rod, two acrylic plates with holes, gimbal assembly, electronic circuit board, and weights. The assembled CAD model, as well as the fabricated CMBS, are shown in Figure 4-2a and b. The basic idea behind the CMBS is that by positioning some extra weights around the circular plates, the COM can be moved to the desired point to improve the stability of the end-effector. To have an adequate flexibility and resolution for positioning the weights, a circular pattern of holes is machined on two 50 mm diameter and 3.2 mm thick acrylic plates.

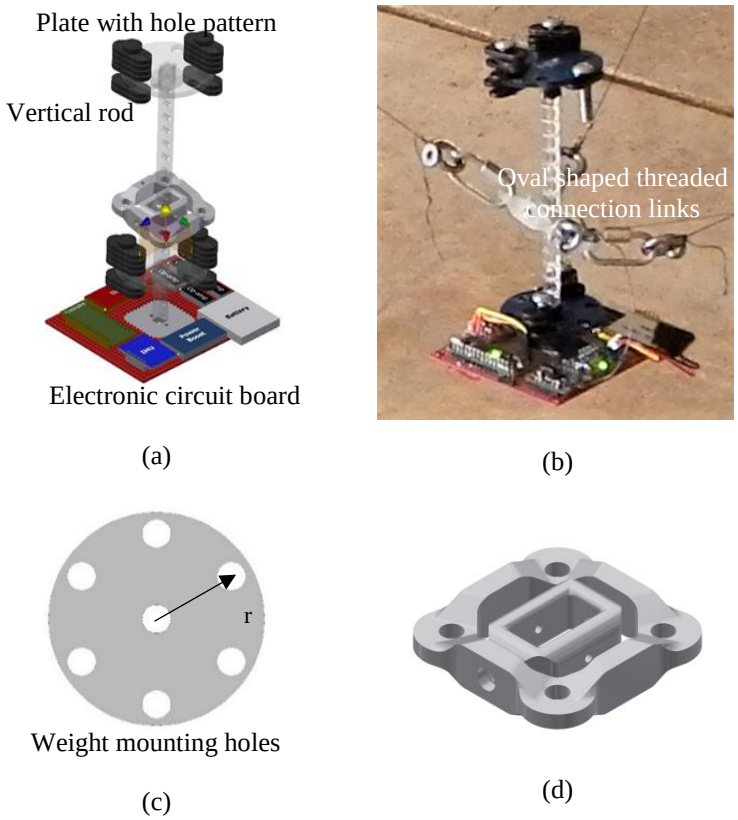

Figure 4-2: a) CAD model of the CMBS; b) Assembled CMBS c) Circular plate for weight mounting; d) gimbal system

One plate is positioned above the cable connection point while the other is positioned below. Both plates are designed to allow for an adjustable offset from the cable connection point

(Figure 4-2.c). The top plate can be used to enhance the stability of the end-effector when the end-effector's COM is below the cable's connection point with or without horizontal offset, and the COM must be shifted to the center or near the center. The bottom plate can be used for cases in which the COM is above the cable's connection point with or without horizontal offset. Also, a combination of the two plates can be used to achieve more flexibility in arranging the weights. The weights are each 4.5±0.1 g steel Slide-In T-Nuts that are mounted on the plates using screws, which are each 4.6±0.1 g.

To hold the entire end-effector assembly, cables should be connected to a frame, which is also attached to the vertical rod. To obtain that connection, a gimbal system is designed, and cables are connected via four oval-shaped threaded connecting links (Figure 4-2.b). The gimbal consists of two 3D printed frames: the outer one for the cable connection and the inner one for the vertical rod connection (Figure 4-2.d). Frames are assembled using pins and ball bearings for low friction rotation. The gimbal allows the end-effector to roll and pitch with minimal restriction.

To show how the CMBS works, it is necessary to determine the position of the COM in the end-effector before and after using the CMBS. There are two simple methods, which can be used to find the position of the COM in the end-effector. In the first method, which is used in this research, the mass of each part and sensor is measured and assigned to the corresponding part in its CAD model. Since the sensors are small and light-weight relative to the other parts of the system, the COM for each sensor is assumed to be in the center of its volume. The parts are then assembled in the software, and the position of the COM of the entire assembly is calculated using a toolbox in Autodesk® Inventor™ 2017.

In the second method, the center of mass of the whole end-effector, or each part separately, can be measured using a force measuring platform, which consists of four load cells, a frame or

structure for placing the object, and an electronic circuit board for exporting the load cells' data. Figure 4-3 shows the schematic design of a COM finder apparatus. In this device, an object is placed on the device's top plate, and the force of each load cell is measured. Per the equilibrium equations of Newton's second law, the center of mass can be determined. The force equilibrium equation in the y-direction calculates the object's mass. The coordinates of the COM in the x-z plane can be measured by means of the torque equilibrium equations around the x and z-axes. In the current orientation of the object shown in Figure 4-3a, the coordinates of the COM can only be measured in the plane 1. To find the position of the COM in the plane 2, the object should be oriented around the z-axis and be placed on the device plate with the adjacent face corresponding to plane 2 (Figure 4-3b).

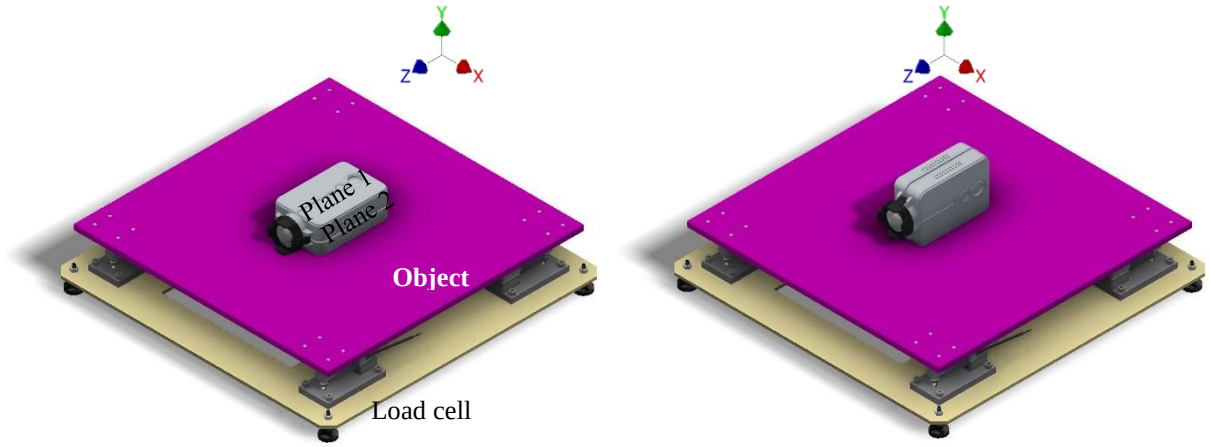

(a) (b)

Figure 4-3: COM finder apparatus

This method is appropriate for irregularly shaped objects with non-homogeneous mass distribution. Therefore, the position of each sensor or part can be measured by this device and the COM of the whole system can be calculated by the equation for finding the center of mass of a system of particles.

In the case of a system of n particles, each with mass m, located in space with coordinates $\bar{r}$ and a center of mass located at the coordinates $\overline{R}$, the following condition must be satisfied.

$$\sum_{i=1}^{n} m_i(\overline{r_i} - \overline{R}) = 0 \tag{4-1}$$

solving (4-1) for $\overline{R}$ yields

$$\overline{R} = \frac{1}{M}\sum_{i=1}^{n} \overline{m_i r_i} \tag{4-2}$$

where M is the total mass of all particles.

The calculated COM position of the end-effector before using the CMBS is 58 mm below the gimbal pivot with 4.1 mm offset from the axis of symmetry. By moving the circular plates along the vertical rod and positioning the weights around the holes' pattern of circular plates, the COM position can be shifted to the desired position. To obtain this, certain parameters need to be calculated first, such as the distance of each plate from the gimbal pivot, the desired hole for mounting the extra weight, and the number of extra weights to be placed in the hole. To do this, the same principle can be used as discussed before for finding the COM of the end-effector using equation (4-2).

For instance, in the current CMBS, it can be assumed that the origin is located at the gimbal pivot, and the COM of the end-effector before mounting the weights is at $G(a, b, -c)$ (Figure 4-4). Therefore, to move the COM to the origin, the required weight (m), its position on the circular plate (r, θ), and the plate's distance from the origin (h) can be found from equation (4-2).

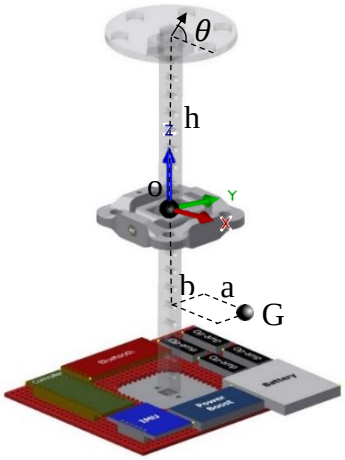

Figure 4-4: An example of the COM position for CMBS calculations

To begin with, the COM needs to be moved to the axis of symmetry, $(x, y) = (0,0)$. It is essential to do this because the gimbal system cannot restrain roll and pitch, and it tilts if any torque is applied to it. Thus, rewriting equation (4-2) for the x and y directions, respectively and considering R_x=R_y=0, yields:

$$\frac{m_2 \cdot r \cdot \cos(\theta) + a \cdot m_1}{m_1 + m_2} = 0 \tag{4-3}$$

$$\frac{m_2 \cdot r \cdot \cos(\theta) + b \cdot m_1}{m_1 + m_2} = 0 \tag{4-4}$$

where m_1 is the weight of the end-effector before mounting weights, and m_2 is the total weight of the extra mass. Dividing equation (4-4) by (4-3) yields:

$$\tan(\theta) = \frac{-a}{-b} \tag{4-5}$$

$$\theta = 180 + \tan^{-1}(\frac{a}{b}) \tag{4-6}$$

which means that the weight should be mounted symmetrically to the COM. To find the required weight, the θ obtained from equation (4-6) must be substituted into either equation (4-3) or (4-4). Substituting equation (4-6) into (4-3) yields:

$$m_2 = \frac{a \cdot m_1}{r \cdot \cos\left(\tan^{-1}\left(\frac{a}{b}\right)\right)} \tag{4-7}$$

In this relation, m_2 is inversely proportional to r. It means that for minimizing the number of extra weights added to the system, the radius of the hole plate should be as large as possible. However, a very large hole plate may block the sunlight or add to the weight of the system.

To determine the distance of the plate from the origin (h), the same method can be used for the z-direction. Therefore, rewriting equation (4-2) in the z-direction and considering R_z=0 yields

$$\frac{m_1 \cdot c + m_2 \cdot h}{m_1 + m_2} = 0 \tag{4-8}$$

solving (4-8) for h yields

$$h = \frac{m_1 \cdot c}{m_2} = \frac{m_1 \cdot c}{\frac{a \cdot m_1}{r \cdot \cos(\theta)}} = \frac{r \cdot c \cdot \cos\left(\tan^{-1}\left(\frac{a}{b}\right)\right)}{a} \tag{4-9}$$

As can be seen in the relation (4-9), the distance h is inversely proportional to m_2. It means decreasing the number of extra weights would increase the distance of the plate from the gimbal pivot and consequently increase the size of the end-effector. Therefore, an optimum amount of extra weight should be used so as to limit the increase in weight and size of the end-effector. To obtain the optimum values for weights, there are different parameters, which depend on the design specifications of the 4CDPM, such as the maximum load that can be tolerated by the system as well as the limitations for enlarging the size of the end-effector. For instance, casting more shadow on the crop with a large end-effector or increasing wind drag, which may contribute to more vibration. However, with known design constraints in the full-size system, the required number of weights and their position on the end-effector can be easily determined using equations (4-6), (4-7), and (4-9).

To help researchers find the best place for putting the extra weights, a computer program can be used to automate finding the COM. The computer program uses the output data from the COM finder apparatus for its input in order to calculate the number of extra weights and their coordinates on the hole plates (Figure 4-5). To facilitate positioning, each hole on the plate can be numbered. Therefore, researchers just need to place the weights in the specific hole number suggested by the computer program. It is important to mention that the extra weights are not necessarily extra masses imported to the system. They can be batteries or other sensors whose position does not affect data collection, such as a communication center or data logger. The COM finder apparatus and computer program need to be designed and tested in future research.

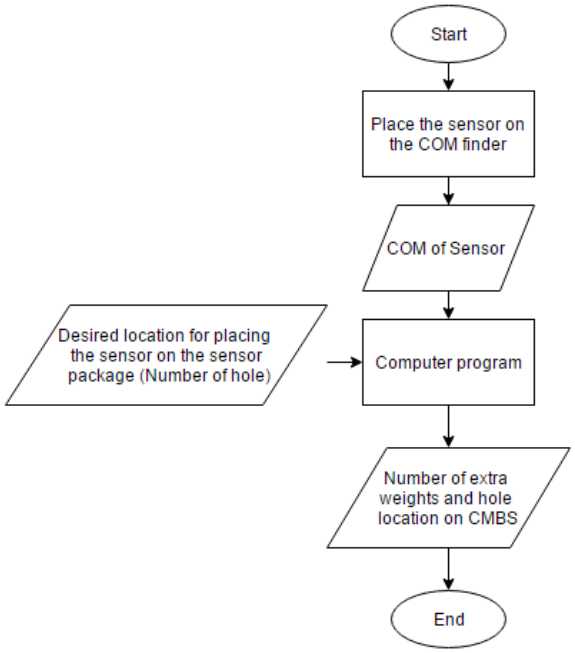

Figure 4-5: Process for efficiently determining the ideal location for putting the extra weights

4.1.2 Sensor package

The sensor package for measuring the orientation of the end-effector and the tension in the supporting cables is composed of various devices (Figure 4-6). (e.g. a microcontroller, an inertial measurement unit (IMU), a Bluetooth modem, and a power supply). Power is supplied by a single-

cell 500 mAh lithium ion battery. To supply an appropriate voltage for the components, the battery is connected to a 5V power boost. The 5V output is used as the main power source for all other components. The Adafruit Metro Mini 328 serves as the microcontroller for the IMU and load cells. The Metro Mini offers a compact size to minimize the device's influence on the end-effector COM while maintaining appropriate utility for all accompanying components. The Adafruit BNO055 absolute orientation sensor was chosen as the IMU for this device. It transfers data to the Metro Mini through ISP communication and comes with its sensor fusion algorithm for taking accurate orientation measurements. All data is sent to and stored on a laptop running a Python program. The data are transferred with a SparkFun BlueSMiRF Bluetooth modem.

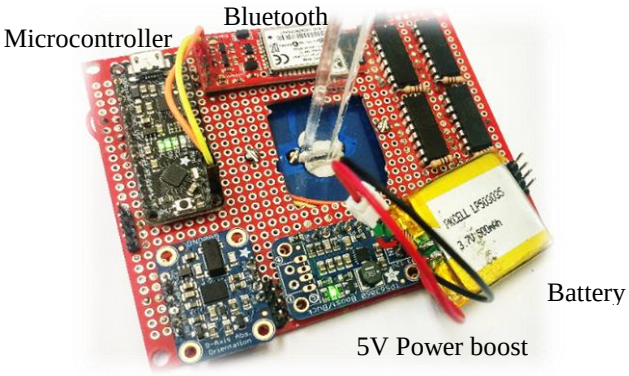

Figure 4-6: Electronic circuit board for the sensor package

4.1.3 12th-Scale four-cable driven manipulator

The experimental model used in this research is a 12th-scale hardware of the desired full-scale system (Figure 4-7). Dyneema fishing line (0.6 mm diameter) is actuated utilizing custom, miniaturized winches. Tripodal towers are used in place of guyed poles to allow for both rigidity and mobility of the support structures. Each winch assembly is controlled via RF communications with the system controller interface and run off of individual power supplies to allow the system to be easily repositioned and scaled. Due to the reduced scale and cost of implementation, Differential Global Positioning System (DGPS) is not used for position tracking. Rather, winch

encoders are used to track cable lengths from which the end-effector position may be approximated.

Figure 4-7: 12th-Scale four four cable driven manipulator

4.2 Experiment procedure

To assess both the functionality of the CMBS and the effect of the COM on the stability of the end-effector, two sets of experiments (so called “balanced” and “unbalanced”) are performed on the 12th-scale end-effector in a 12th-scale four cable-driven parallel manipulator. In the unbalanced case, the end-effector’s COM is moved to 33 mm under the gimbal pivot on the axis of symmetry. In the balanced case, the COM is moved to the pivot point on the axis of symmetry. The position of the COM for three cases of the balanced and unbalanced end-effector, and without using the CMBS is shown in Figure 4-8. As shown in Figure 4-8a, the COM had a small horizontal offset, which is removed after using the CMBS.

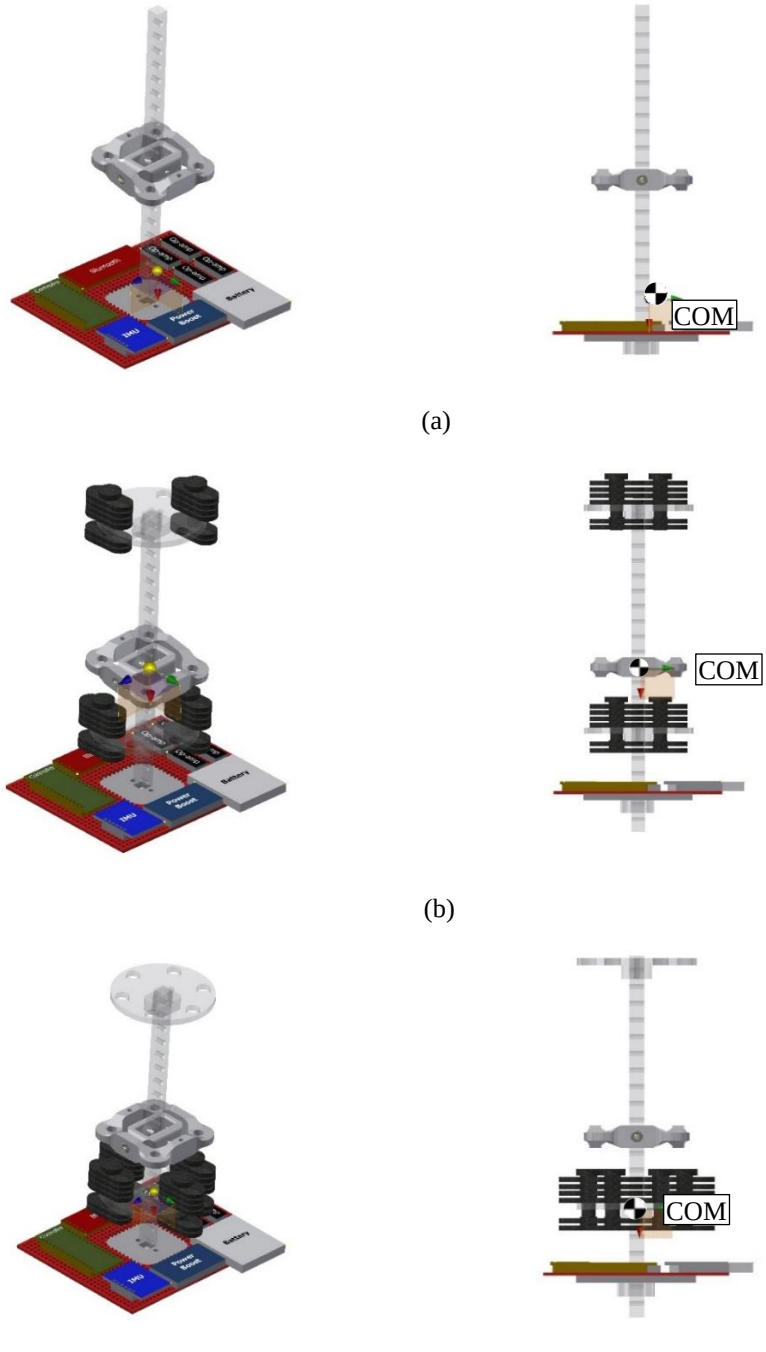

(a)

(b)

(c)

Figure 4-8: Position of COM in a) not using CMBS (58 mm below gimbal axis); b) using CMBS to move the COM onto the gimbal axis to the **balance** the end-effector; c) using CMBS to move the COM to 33 mm under the gimbal axis for the **unbalanced** test.

In each set of experiments, the end-effector is tested at the four points of the field at two different heights of 41 cm and 82 cm above the ground. These two heights are 12^{th}-scale of the full-scale system operation height of the end-effector where the end-effector is located above the

canopy surface and at the maximum height, which was mentioned in Table 2-1. As can be seen in Figure 4-9, at each point the direction of moving the end-effector towards that point is imaged. The experiments are carried out only in one-quarter of the field because of the symmetric geometry of the system. For example, at point 1 (center), the end-effector is placed to the left side of point 1, close to point 2, and moved to the center from left to right using a custom controller. The same procedures are used for moving it from front to back. In each case, the sensors collected the orientation and tension data and transmitted the data to the computer via Bluetooth from the start of movement until the end-effector stops at the designated point and vibration settles down significantly. In these tests, the pitch and roll rotation data are collected from the IMU. To maintain the consistency of the experiment in terms of the collected roll and pitch data, the end effector is always connected in the same orientation as can be seen in Figure 4-10.

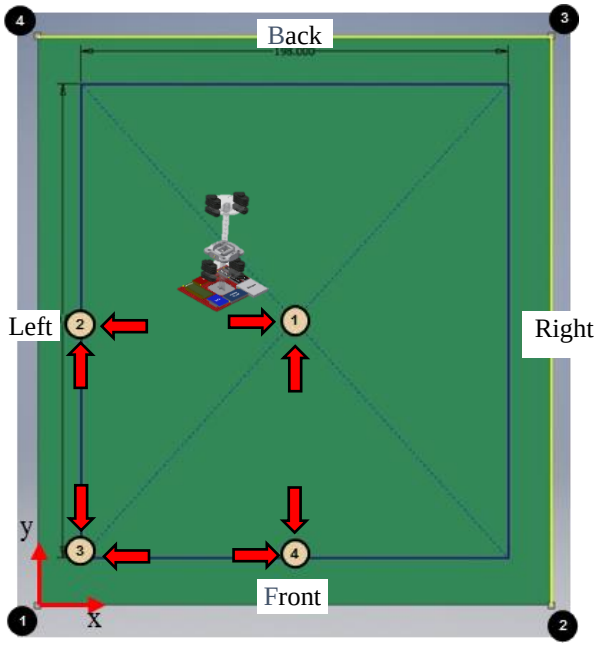

Figure 4-9: Top view of 12th-scale field

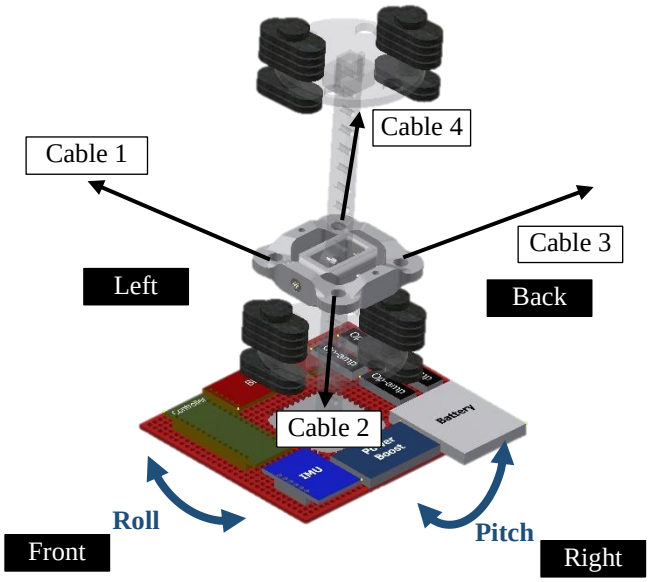

Figure 4-10: Orientation of the end-effector in the 12th-scale 4CDMR and rotation directions

A representative example of acquired IMU data is shown in Figure 4-11 for point 1 at the height of 41 cm moving from left to right both in the balanced and unbalance experiments. In these diagrams, the oscillation amplitude of the end-effector versus time is shown for the pitch and roll rotation.

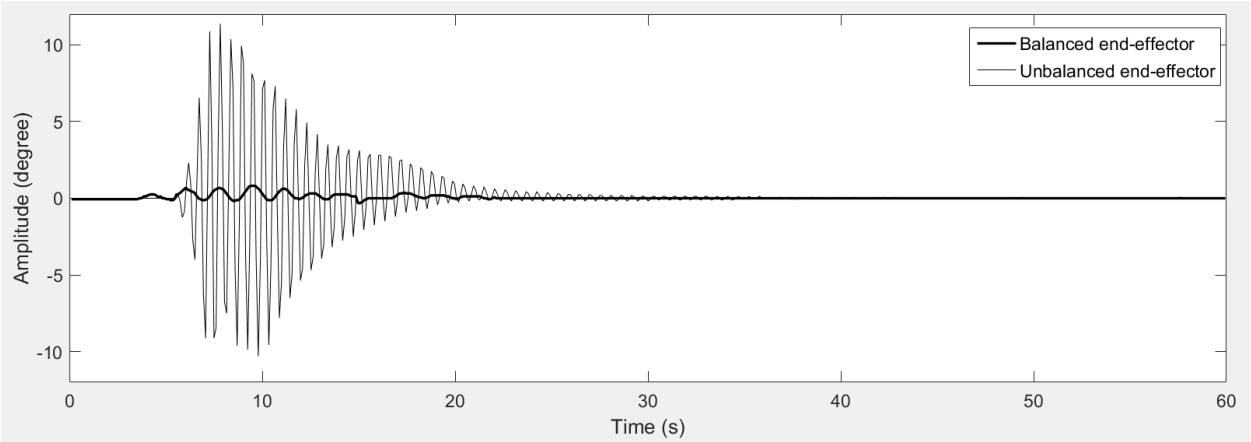

(a) Pitch orientation

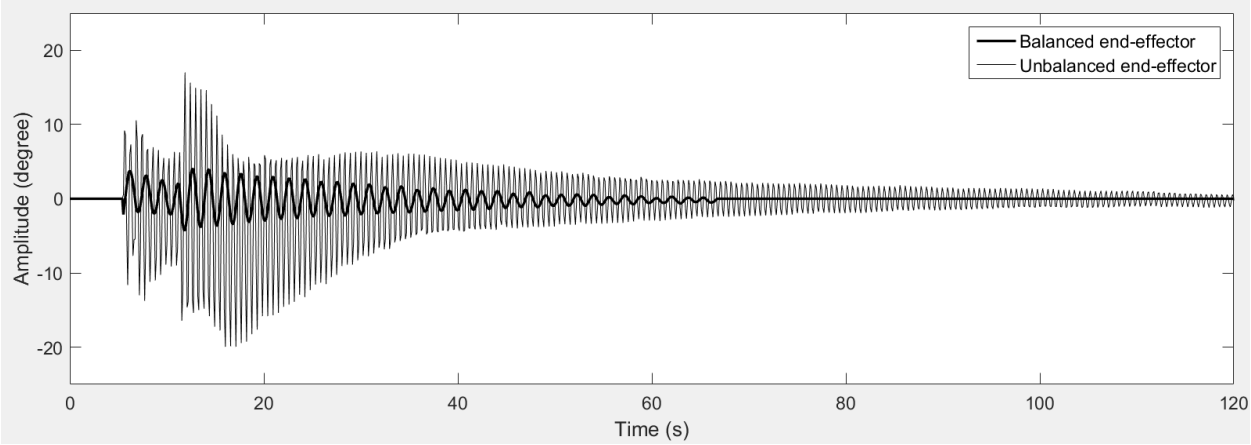

(b) Roll orientation

Figure 4-11: Acquired IMU data for point 1 at 41 cm height moving from left to right both in the balanced and unbalanced experiment. a) Pitch orientation; b) Roll orientation

Table 4-1 shows an example of the results for the maximum amplitude of motion and maximum frequency of the vibration for point 1. The complete table for all the points can be seen in Appendix 1.

Table 4-1: Vibration experiment for balanced and unbalanced end-effector in point 1

			Pitch		Roll	
Point number	Moving direction	COM	Maximum Frequency (Hz)	Maximum Amplitude (degree)	Maximum Frequency (Hz)	Maximum Amplitude (degree)
1	High Front to Back	Balanced	0.6	3.125	0.61	0.6875
		Unbalanced	1.83	10.125	1.81	2.18
	High Left to Right	Balanced	0.573	0.5	0.611	3.125
		Unbalanced	1.82	2.93	1.831	13.98
	Low Front to Back	Balanced	0.612	5.5	0.572	0.75
		Unbalanced	1.82	14.6	1.814	3.68
	Low Left to Right	Balanced	0.573	0.687	0.613	4.06
		Unbalanced	1.832	11.375	1.834	19

The results can be verified by the equation of natural frequency in a compound pendulum.

$$\omega_n = \sqrt{\frac{MgR}{I}} \tag{4-10}$$

where I is the moment of inertia of the pendulum about the pivot point, M is the total mass of the pendulum, and R is the distance between the pivot point and the center of mass. In our experiments since the balance end-effector has a very small R, the frequency of the pendulum is smaller than the unbalance end-effector with larger R. Also I for the balance end-effector is approximately twice of the unbalance end-effector. Higher moment of inertia decreases the natural frequency in equation (4-10). Higher amplitude of motion in the unbalance end-effector is because of the large COM distance from the pivot point (R). Large R creates a long torque arm causing the end-effector to vibrate with high amplitude when the end-effector suddenly stops at one of the four experiment locations.

4.3 Results and Discussion

The end-effector was tested at eight points in the field for two cases of balanced and unbalanced end-effectors. In each test, the end-effector was moved to one of the eight points and stopped suddenly to induce vibration due to its momentum. The orientation data then were collected to show the effect of the COM on the stability of the end-effector (Appendix 1). The comparison between the two cases of balanced and unbalanced end-effector indicates that in all the tests, the amplitude of motion and maximum frequency is higher for the unbalanced end-effector than for the balanced one. Because in the unbalanced case, the COM is under the rotation pivot and the end-effector has undergone a pendulum effect. When the end-effector stops at one of the eight points, the momentum creates the pendulum effect, causing the end-effector to oscillate about the center of rotation. The average calculated frequency for the balanced case for all eight points is 0.57 Hz and for the unbalanced case is 1.83 Hz, which is more than three times higher

than the balanced end-effector. In addition, the average amplitude of oscillation for the balanced case is 1.94 degrees and for the unbalanced case is 6.86 degrees, which is approximately four times higher than the balanced end-effector.

4.4 Conclusion

The sensor package is one of the most important parts of the end-effector in the 4CDPM. It consists of a variety of sensors and electronic devices with different sizes and weights. Researchers sometimes need to add, remove, or swap sensors in the sensor package to reach their imaging and radiometric data acquisition goals. Any changes in the position of objects inside the sensor package can alter the COM of the whole end-effector, resulting in instability during movement or extra force on the gimbal and stabilization system. To prevent this, an easy to use passive system (the so-called center of mass balance system) was designed and tested, which enables researchers to simply add or remove components to the sensor package. This passive system uses two circular plates with a pattern of holes for weight attachment and a rod for mounting the circular plates at different heights. A combination of weight arrangement with plate movement along the vertical rod provides enough resolution for COM adjustment. Researchers can use the proposed COM finder apparatus and automated computer program to find the best location for the placement of weights on the CMBS. A larger plate with more holes can provide a higher resolution system with more flexibility for balancing the COM. The CMBS also has some limitations. First, the total weight of the end-effector after mounting the extra weights should not exceed the maximum designed weight of the 4CDPM. For example, batteries and communication center can be used as the extra weights. Second, size of the hole plate needs to be selected carefully to avoid casting shadow on the plants.

Moreover, in this research two series of experiments were performed, first to see the influence of the COM offset on the static and dynamic equilibrium of the end-effector and also to prove the functionality of the CMBS. The experimental results show that the COM position plays a major role in the dynamic performance of the 4CDMR end-effector. Due to the use of a gimbal system, the COM should always be on the axis of symmetry of the end-effector; otherwise, an external moment is applied on the gimbal, causing the end-effector to tilt. Also, the positioning of the COM in the axis of symmetry is important as well. A COM below the center of rotation causes the system to experience higher vibration frequency and greater amplitude of motion than a balanced system, in which the COM is located at the gimbal pivot. In conclusion, the proposed CMBS easily and intuitively moves the COM position to the axis of symmetry or the gimbal pivot, to reduce the pendulum effect and undesired orientations.

Part II: Drop Down System (DDS)

Chapter 5 : Introduction and Motivation

As discussed in Chapter 1 of Part I, plant remote sensing is the process of obtaining electromagnetic radiation information about an object without coming into direct contact with the object [12]. In this process, biophysical features of plants can be characterized spectrally using various imagers and sensors that are integrated into the remote sensing sensor package.

Field personnel use remote sensing systems and technologies to obtain agricultural information as a diagnostic tool in the site-specific management of crops [72]. Remote sensing can be divided into three categories: ground-based, airborne and satellite [73]. A system which is able to support all of these categories at the same time is known as a comprehensive system. In other words, a comprehensive, fully integrated remote sensing system analyzes the crop status at various scales of investigation ranging from the leaf level to the regional satellite level [24]. High remote sensing quality and thorough spectral data of certain areas can be collected using a comprehensive system.

The current 4CDPM can collect spectral data at the field and canopy levels. It also has a limited capability to scan the plants at the leaf level, but only for the top-level leaves at the canopy surface that are located underneath the sensor package. This limitation is due to the fact that the 4CDPM end-effector cannot be lowered under the canopy surface; otherwise, the four support cables (and the dolly itself) may impinge upon crops surrounding those being imaged. Therefore, a system needs to be designed to enable researchers collecting spectral data under the canopy surface at the leaf level. This system also can be used for studying soil and vegetation near the ground surface. It is important to collect spectral data from an area close to the ground to be truly representative of the soil, and target vegetation in low height [74]. The technique of dropping a subsystem from the main end-effector for collecting ground level data was used before in other

research projects. An autonomous aerial water sampling system at the University of Nebraska-Lincoln was developed, which uses a lowered sub-system with two tubing systems for sampling the water from a lake or river (Figure 5-1) [75]. A similar system is also used by Amazon Company to deliver shipments to their customers in the shortest possible time. Figure 5-2 shows a tether system proposed by Amazon that lowers packages to the ground from a drone [76].

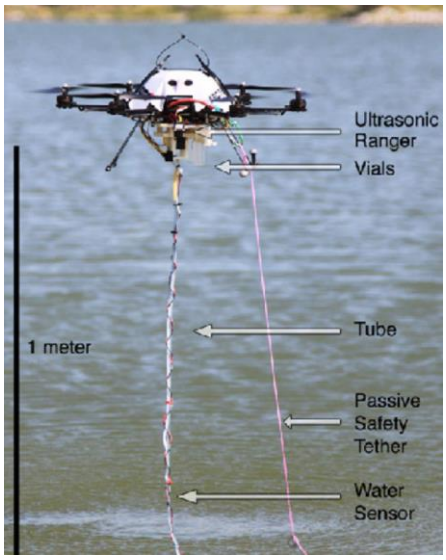

Figure 5-1: UAV-based water sampling

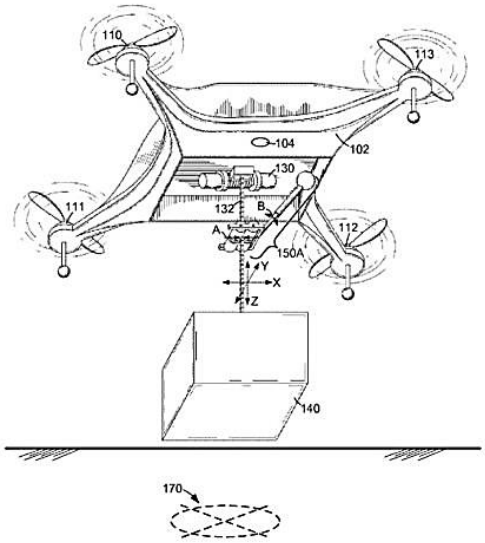

Figure 5-2: An Amazon sketch shows a tether system to lower packages to the ground

Therefore, the purpose of the second part of this thesis is to determine the feasibility of a dolly subsystem that noninvasively lowers a second phenotyping sensor package into the canopy. This system is called a Drop-Down System (DDS) here after.

Chapter 6 takes a closer look at the mathematical analysis of a two-dimensional DDS. In addition, a dynamic simulation of a small size computer model is performed in CAD software, and the result is compared to the experimental result of a similar physical model in order to validate the accuracy of the software's result. In Chapter 7, a full-size model of the DDS is designed in the CAD software, and several dynamic experiments are carried out. In these experiments, the vibration sensitivity of the DDS is analyzed in various conditions. Also, in this chapter, a preliminary feasibility of the DDS concept is determined. Chapter 8, focuses on developing a preliminary 12^{th}-scale DDS prototype as a primary system for future developments. Finally, the conclusion chapter describes the future work associated with the devices as well as the accomplishments achieved through the design of each device.

Chapter 6 : Initial prototype and dynamic modeling

A Drop-Down System (DDS) is a supplementary module, which enables the researchers to analyze small height crops in the field where the main sensor package of the 4CDPM is not able to go. This system consists of a small sensor package, which is moved into the canopy while the dolly and the main sensor package are placed in the proximity of the canopy surface.

Wind force and the reaction forces of struck plants are two primary potential disturbances of this system. The pendulum effect caused by the suspended small sensor package is one of the consequences of these disturbances, which makes the entire end-effector unstable. An unstable system can make the sensing and imaging of the canopy hard to perform. Moreover, an unstable system needs more support from the active stabilization system, which results in more energy consumption from the batteries.

In general, the effective parameters in designing the DDS are the lowered height, the weight of the small sensor package, the magnitude of the external disturbances, and the stiffness and the damping ratio of the system. The purpose of this chapter is to determine the dynamic response of a two-dimensional DDS to different inputs as a starting point for studying the dynamics of the three-dimensional system. In this chapter, also, a small scale three-dimensional DDS is modeled in the computer software, and the results are compared with an identical physical model.

6.1 Two-dimensional DDS model

Figure 6-1 shows a simple two-dimensional model of the DDS, which has three degrees of freedom. The vertical bar is completely connected or welded to the horizontal bar at one end and welded to the sensor package at another end. Two systems of spring and damper are attached to

the horizontal bar which have the stiffness and damping constant of k and c respectively. The angle of rotation is shown by α and the angle between each cable and the cable connection support (w) is shown by β_i. The weight of the cable connection support (horizontal plate), lowering rod, and small sensor package are M_1, M_2, and M_3 respectively. The length of the cable connection support and the lowering rod are W and d1. The small sensor package is assumed a square with a side length of d_2. The wind force and other possible disturbances are shown by F_1 and F_2. The center of mass is located at point G, whose exact position from the x-y origin (D) can be determined using the following equation.

$$D = \frac{M_2 \frac{d_1}{2} + M_3 \frac{d_2}{2}}{M_1 + M_2 + M_3} \tag{6-1}$$

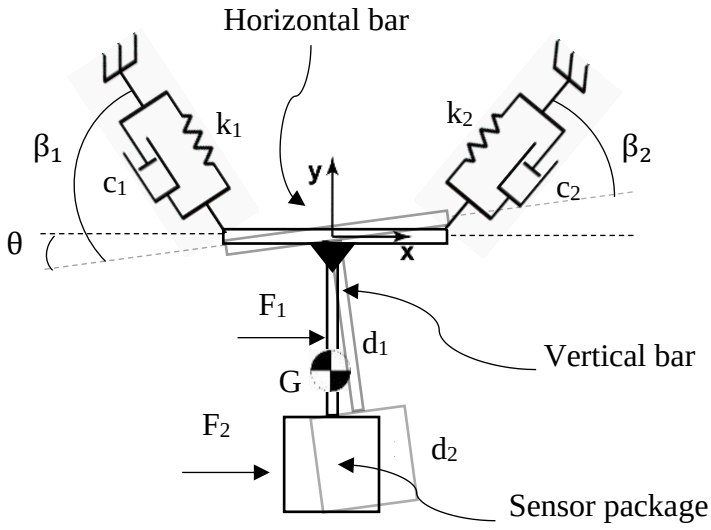

Figure 6-1: Two-dimensional model of the DDS

Assuming the DDS is a single rigid body, the free-body diagram of this system, after a small positive counterclockwise rotation and positive translation in the x and y-direction, is shown in Figure 6-2.

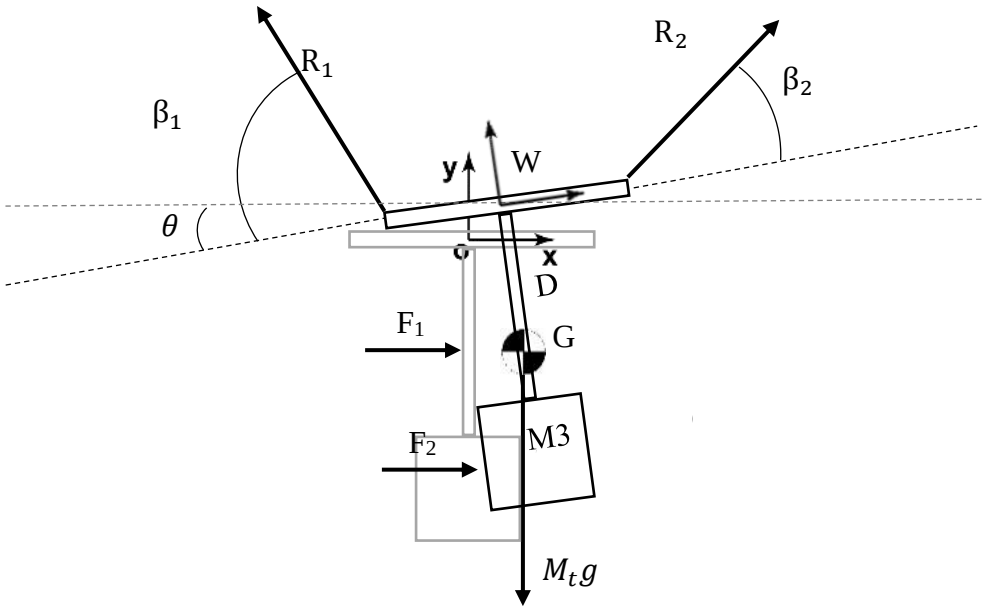

Figure 6-2: DDS after a small positive counterclockwise rotation and positive translation in x and y-direction

In this model, Mt is the total mass of the system. R1 and R2 are the total force of each cable due to damping and cable stiffness. Since cables are replaced by a system of spring and damper, the required force to extend or compress a spring (R_k) obeys the Hooke's law. Also, the frictional force R_f can be modeled as being proportional to the velocity v of the object: $R_f = -cv$, where c is the so called "viscous damping coefficient." According to the geometry of the problem and assuming the cables are always in tension, the cable's length change for each cable can be written as below:

$$\Delta l1 = L1 + x\ \cos(\beta_1 - \theta) - y\ \sin(\beta_1 - \theta) + \frac{w}{2}\alpha\ \sin(\beta_1 - \theta) \quad (6\text{-}2)$$

$$\Delta l2 = L2 - x\ \cos(\beta_2 + \theta) - y\ \sin(\beta_2 + \theta) - \frac{w}{2}\alpha\ \sin(\beta_2 + \theta) \quad (6\text{-}3)$$

where Δl1 and Δl2 are the length change in cables 1 and 2. The translational movement of the DDS in the x and y-direction are x and y respectively. Using the Hooke's law and friction force relation, the total force of each cable can be found as:

$$R1=k\,\Delta l1+c\,\frac{d(\Delta l1)}{dt} \tag{6-4}$$

$$R2=k\,\Delta l2+c\,\frac{d(\Delta l2)}{dt} \tag{6-5}$$

Applying the three equations of motion gives the dynamic equations for the DDS:

$$\sum F_x = M_t\bar{a}_x \Rightarrow R2\cos(\beta_2+\theta) - R1\ \cos(\beta_1-\theta) = M_t\bar{a}_x \tag{6-6}$$

$$\sum F_y = M_t\bar{a}_y \Rightarrow R2\sin(\beta_2+\theta) + R1\ \sin(\beta_1-\theta) - M_t g = M_t\bar{a}_y \tag{6-7}$$

$$\sum M_G = \bar{I}\ddot{\theta} \Rightarrow D\times R2\cos(\beta_2) - D\times R1\ \cos(\beta_1) - \frac{w}{2}\sin(\beta_2) + \frac{w}{2}\sin(\beta_1) = \bar{I}\ddot{\theta} \tag{6-8}$$

where D is the distance between the center of mass and the origin, and $\bar{I}$ is the mass moment of inertia. β_1 and β_2 are assumed to be constants in each position of the field that the end-effector is positioned.

Depending on the position of the end-effector in the field, equations (6-6) to (6-8) are nonlinear equations, and each includes three variables of x, y, and θ. Because of the complexity of solving these equations on the one hand and the over simplified representation of DDS in 2D on the other hand, a simple small-size physical 3D system is built, and an identical computer model with the same size and feature is created in Autodesk Inventor 2017. The reason for performing computer modeling and comparing it with the physical model is to verify that the software is accurate enough for performing future 3D simulations without requiring a physical model to obtain the dynamic results.

6.2 Small scale three-dimensional DDS model

Figure 6-3a shows a small scale computer model of the DDS, which is designed in the CAD software. Figure 6-3b shows the same physical model of the system. The stiffness and damping constant of each spring are 33.75 N/m and 0.026 N s/m respectively. Poles are each 46 cm and the field area is 52 cm × 47 cm.

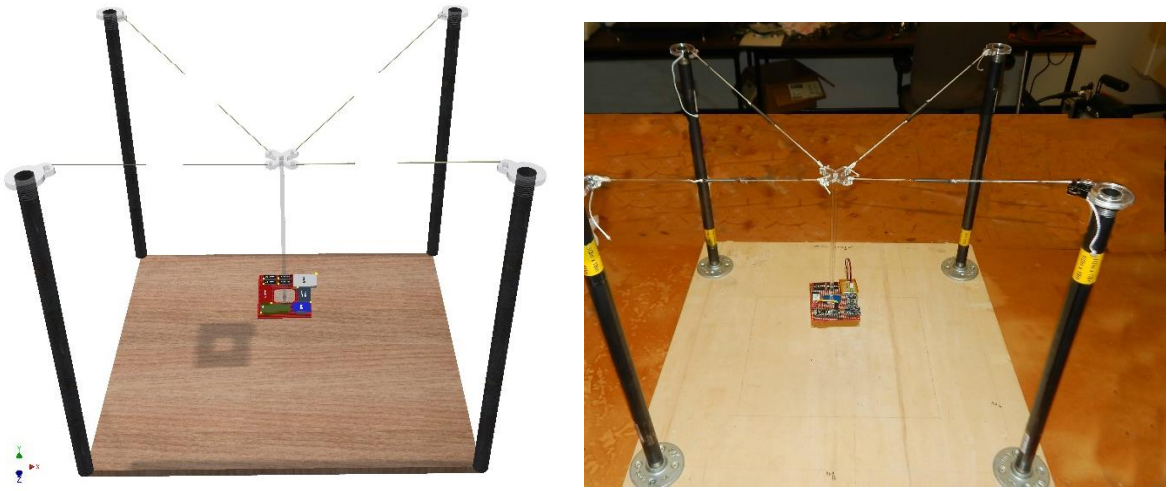

Figure 6-3: a) CAD model of DDS; b) Identical physical model of DDS

In both systems, the cables are connected to the end-effector using a small machined acrylic plate (Figure 6-4), which has four holes for tying the cables. The cables are also tied to the poles, which result in no change in the length of the cables during the experiment. For a better result, the weight and size of each element in the computer model are assigned identical to the physical model. A 25 cm acrylic rod is used to connect the sensor package to the cable connection plate.

A sensor package is used for measuring the orientation of the end-effector and is composed of various electrical elements (Figure 6-5). The main components of the sensor package are a microcontroller and an inertial measurement unit (IMU). Power is supplied by a single-cell 500 mAh lithium-ion battery, and it is connected to a 5V power boost to supply an appropriate voltage to the components. The Adafruit Metro Mini 328 serves as the microcontroller for the IMU. The Metro Mini offers a compact size to minimize the device's influence on the end-effector center of mass while maintaining appropriate utility for all accompanying components. The Adafruit BNO055 absolute orientation sensor was chosen as the IMU for this device. It transfers data to the Metro Mini through ISP communication and comes with its sensor fusion algorithm for taking

accurate orientation measurements. All data are sent to and stored on a laptop running a Python program. The data are transferred with a SparkFun BlueSMiRF Bluetooth Modem.

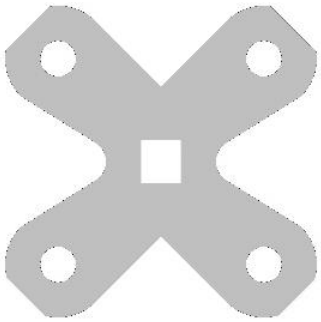

Figure 6-4: Acrylic cable connection plate

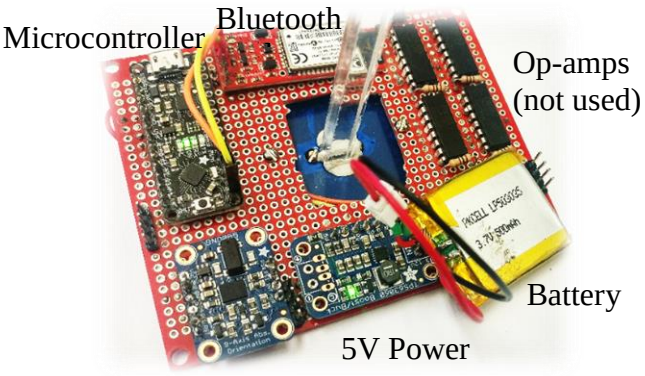

Figure 6-5: Electronic circuit board and sensors

The initial condition for starting the experiment is obtained by putting a 100g weight on the cable connection plate, which lowers the end-effector 3.2cm (Figure 6-6). This initial condition is also applied to the computer model before starting the system to oscillate.

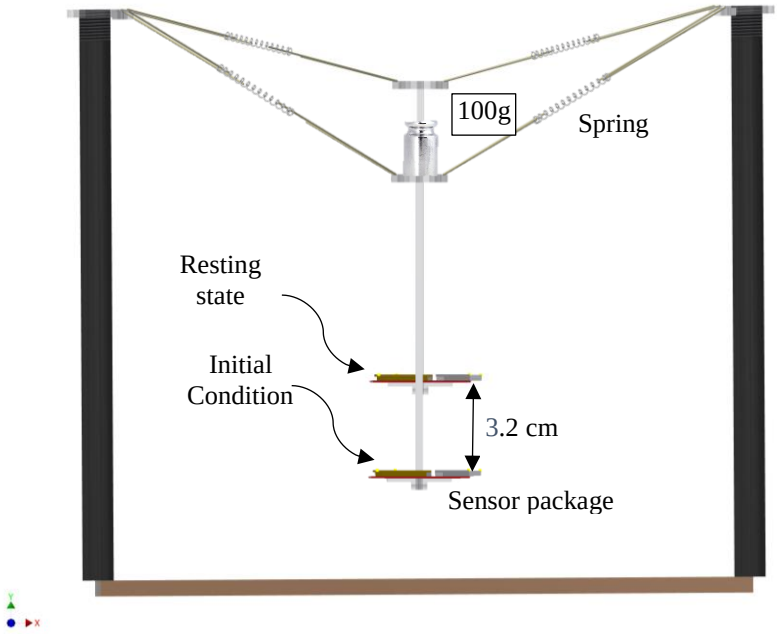

Figure 6-6: Applying the initial condition

The experiment starts once the weight is removed and the end-effector vibrates in the y-direction. Since the initial condition is applied just in the y direction, the movement of the end-

effector in x and z-direction and its rotation around the x, y, and z-axes is close to zero, which is negligible in this study.

The IMU can report acceleration data of the end-effector, but it not capable of indicating an exact coordinate of the sensor in space. Therefore, the acceleration data versus time are collected to be compared to both the computer and physical models. Figure 6-7 shows the results of both the computer and physical experiment.

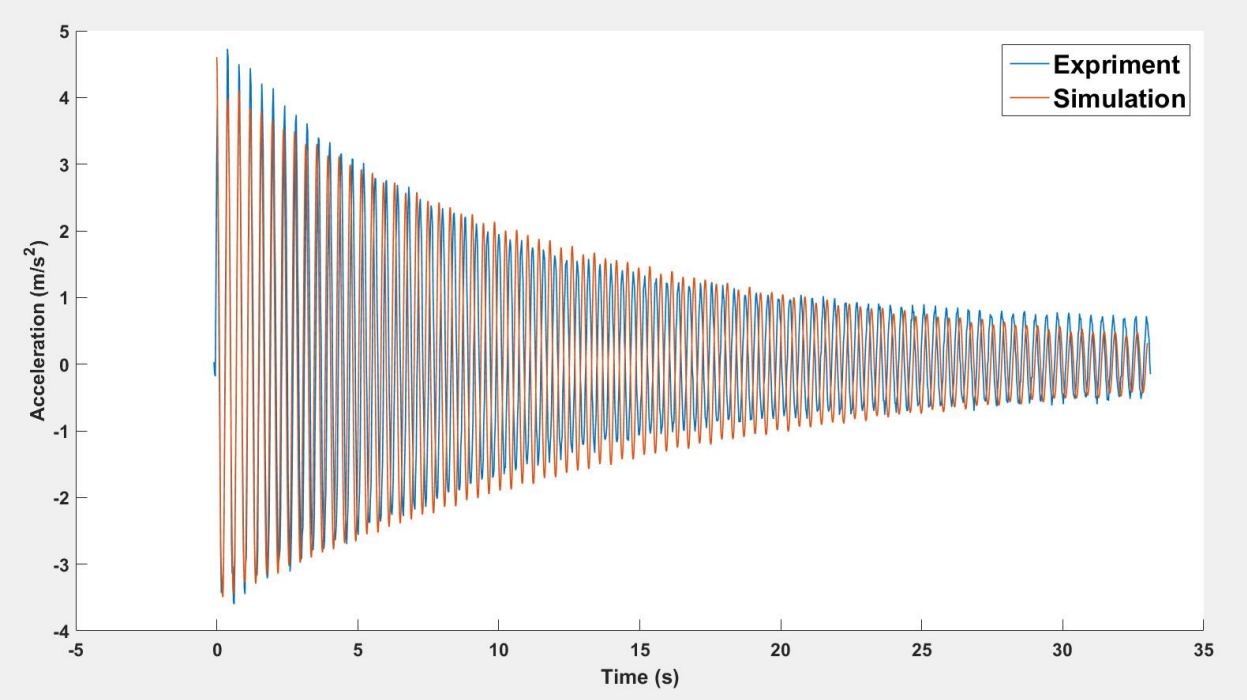

Figure 6-7: The result of computer and physical experiment

6.3 Results and discussion

At the beginning of vibration, both the computer and physical model are identical in frequency and very close in amplitude. After 5 seconds, a small frequency difference is seen in the result of the physical experiment. It is because of the internal damping of ropes and the friction between parts, which are neglected in the computer model. The average frequency for the physical experiment is 2.51 Hz and for the computer simulation is 2.54 Hz. In general, the results show a significant match between the computer and physical experiment, which is a solid validation of

the accuracy of the software's result. Therefore, the software can be used alone for later analysis without requiring the researchers to produce a physical prototype to study the system.

6.4 Conclusion

In this chapter, first, a simple two-dimensional model of a DDS was analyzed. Because of the complexity of solving the equations analytically, a small-scale 3D prototype of the DDS was built, and the vibration data were collected based on an initial condition in the y direction. Then, the result of the physical model was compared to the computer model, which showed a great match between the outcomes of both methods. Therefore, the computer modeling will be used for producing the models and performing dynamic analysis in the future studies in this thesis.

Chapter 7 : Design and Analysis of Full-Scale DDS

A scale model is a physical representation of the full-size system, which maintains the proper relationship between all of the relevant aspects of the model. It demonstrates the behavior or property of the original system without examining the original system. However, it is sometimes hard to scale all of the involved design parameters or conditions. For example, in the 4CDPM, it is hard to scale down the cable specifications. In other words, finding a rope that has an adequate scaled weight, stiffness and damping value is difficult to obtain. In addition, the structure and weight of the cables in the real system can lead to cable sag, which changes the dynamic characteristics of the system. A computer simulation, on the other hand, reproduces the behavior of a system using a mathematical model. It can be used to reduce the cost and time of analyzing the original system significantly. Since the full-size 4CDPM is currently under construction, it will be more cost and time efficient to perform the experiments using the computer simulation. Therefore, Autodesk Inventor 2017 is used for making the CAD models of the entire system and performing the dynamic simulations.

Hence, the purpose of this chapter is to determine the feasibility of a DDS in the full-size version of the 4CDPM. In this chapter, first, a computer simulation is performed to study the effect of disturbances on the operation of the DDS. Next, the feasibility of the DDS is determined by analyzing the sensitivity of the system to different inputs. Sensitivity analysis is a technique used to determine how different values of an independent variable in input can impact a particular dependent variable in output under a given set of assumptions. The DDS is feasible when the input disturbances of the system do not impact the output vibration too much and do not fail the operation.

7.1 Materials and Methods

To perform the simulations, first, a drop-down system (DDS) needs to be designed and mounted on a 4CDPM. In general, the effective parameters in designing a DDS are the lowered height, the weight of the small sensor package, the magnitude of the external disturbances, and the stiffness and damping ratio of the system.

Wind force and the reaction forces of struck plants are two main external disturbances of this system. These disturbances create a pendulum effect in the suspended small sensor package causing the entire end-effector to vibrate and making the sensing or imaging of the canopy hard to perform. Moreover, the active stabilization system would need to consume more energy to stabilize the end-effector.

Several experiments need to be done to examine the effect of the factors mentioned above on the operation of the DDS and accordingly on the stabilization of the four cable-driven parallel manipulator. Therefore, the purpose of these experiments is to explore the vibration sensitivity of the DDS to the design parameters. In other words, the vibration amplitude and speed of the small sensor package is measured based on different inputs.

7.1.1 Full-size 4CDPM

The full size 4CDPM is mounted in a field with an area of 71 m by 80 m. The workspace for the operation of the end-effector is 60 m by 67 m. Poles are each 30 m and are located in the corners of the field as shown in Figure 7-1.

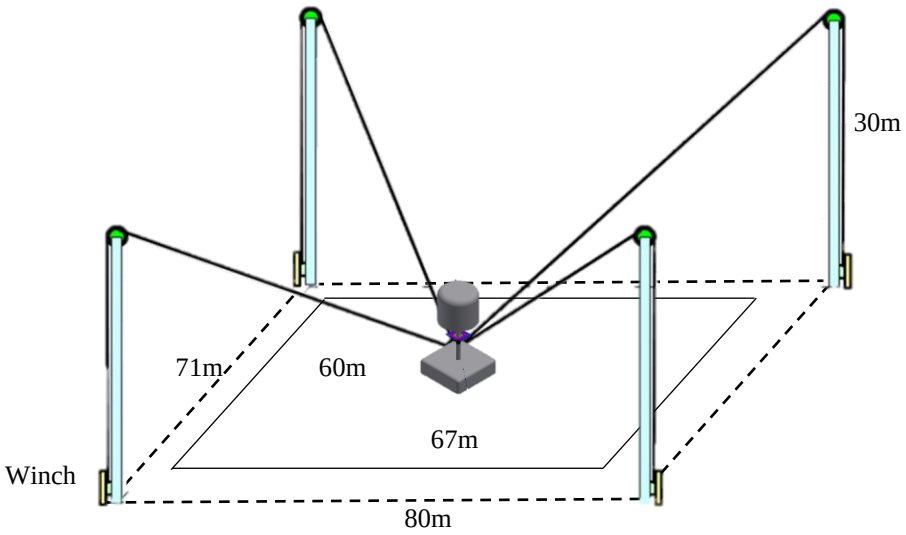

Figure 7-1: Real size phenotyping field for mounting the 4CDPM

7.1.2 End-effector

The end-effector consists of five main parts, each representing a simple demonstration of the real components in the full-size 4CDPM (Figure 7-2). The main end-effector in the proposed computer model has a battery package at the top, a gimbal system with a joint damping constant of 1.5 N m s/deg in the middle, and a large sensor package at the bottom. A solid rod with a variable length ranging from 0 to 5m is used to connect the small sensor package to the main sensor package. This rod is welded to the packages at each end to prevent the small sensor package from rotating around the axis of the rod. Also, it decreases the pendulum effect of the suspended small sensor package by creating a rigid connection. In this study, the weights, stiffness, and the damping ratio of all other components are considered constant values.

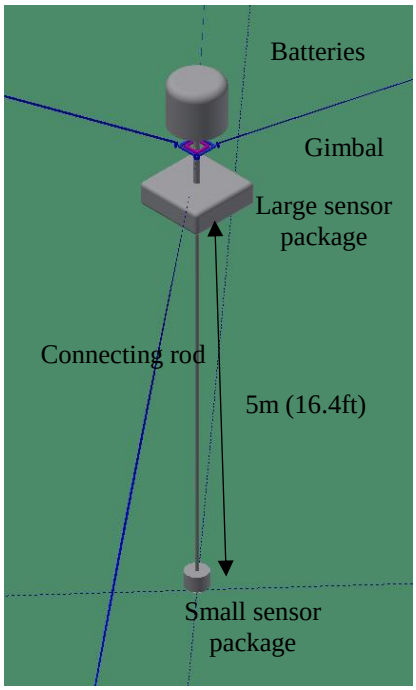

Figure 7-2: The end-effector of 4CDPM

7.1.3 External forces

The magnitude of the external forces is assumed to be at the maximum, based on the worst-case condition, which is 30 mph (13.4 m/s) wind velocity. According to the initial estimations, the weight of the main sensor package and dolly would be at most 130kg, and the weight of the small package is at maximum 10kg. The cables are simulated as long springs without damping with variable stiffness depending on the end-effector position in the field. The stiffness (k) of each cable is modeled as the axial stiffness for an element in tension

$$k = \frac{E\,A}{L} \tag{7-1}$$

where A is the cross-sectional area of the cable, E is the (tensile) elastic modulus (or Young's modulus), L is the length of the cable. For the Kevlar cable, which is used in this system, E is 112.4 GPa, and the cable diameter is 3.6 mm. The length of the cables can be calculated at each point using the distance between the pole tips and the gimbal coordinate in the field.

For sensitivity analysis, the input variables are the lowered height of the small sensor package and the change in the wind drag force due to the change in the projected area of the connecting rod. It is necessary to mention that the maximum height of the maize canopy in this research is 5 m. Therefore, the DDS should travel at most 5 m from the canopy surface to the ground. The drag force is assumed to affect only the small sensor package and the connecting rod, not influencing the large sensor package, batteries, gimbal system, and cables. The relation for calculating drag force is:

$$F_D = \frac{1}{2}\rho V^2 C_d A \tag{7-2}$$

where F_D is the drag force, ρ is the mass density of the air, V is the flow velocity relative to the object, A is the reference area (projected area to surface normal to wind direction), and C_d is the drag coefficient. Both the small sensor package and the connecting rod are modeled as cylinders ($C_d = 0.47$) for simplicity. The diameter and height of the small sensor package are 30 cm and 20 cm. The connecting rod has a 5 cm diameter and variable length from 0 to 5 m.

In the field, wind speed varies continuously, and it is not a constant value. Thus, a white noise signal with a domain of -1 to 1 is used for a better simulation of wind force in the field. The random numbers from this white noise are multiplied by the maximum desired wind speed, which is 30 mph (13.4 m/s) in this study (Figure 7-3). Next, the obtained random wind speed is substituted into equation (7-2) for calculating the wind force.

7.1.4 Computer software

Autodesk Inventor 2017 is a CAD software, which includes a variety of modules for different design purposes. In this study, the dynamic simulation module is used in addition to the part design and assembly module to examine the vibration of the system to the wind force input. With the dynamic simulation or the assembly environment, the intent is to build a functional

mechanism. Dynamic simulation adds to that functional mechanism the dynamic, real-world influence of various kinds of loads to create a true kinematic chain.

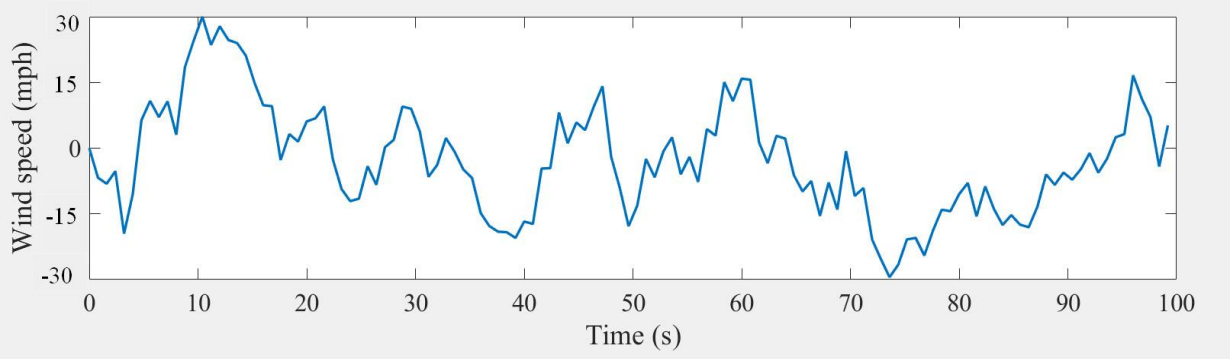

Figure 7-3: A white noise that is used for wind simulation

7.1.5 Experiment procedure

The experiments are done in four positions of the field shown in Figure 7-4 where point 1 has the most symmetric cable tension, and points 2, 3, and 4 have the most asymmetric cable tension. In each position, the drop-down system (DDS) starts working when the main sensor package is placed 5 m above the ground near the canopy surface (Figure 7-5). Therefore, the maximum distance that the drop-down sensor package can travel is 5 m. In each of the four points, the small sensor package starts to move downwards and stops every 0.5m. In each stop, the wind force is applied to the solid rod and the small sensor package for 30 seconds. In this simulation, wind force and weight are applied as external forces, and the cables' tension and the gimbal's damping are applied to the end-effector as internal forces of the system.

Finally, the software calculates the vibration of the small sensor package in three dimensions and stores the vibration amplitude and speed data in separate spreadsheets. A free body diagram of the end-effector is shown in Figure 7-6 for better illustration.

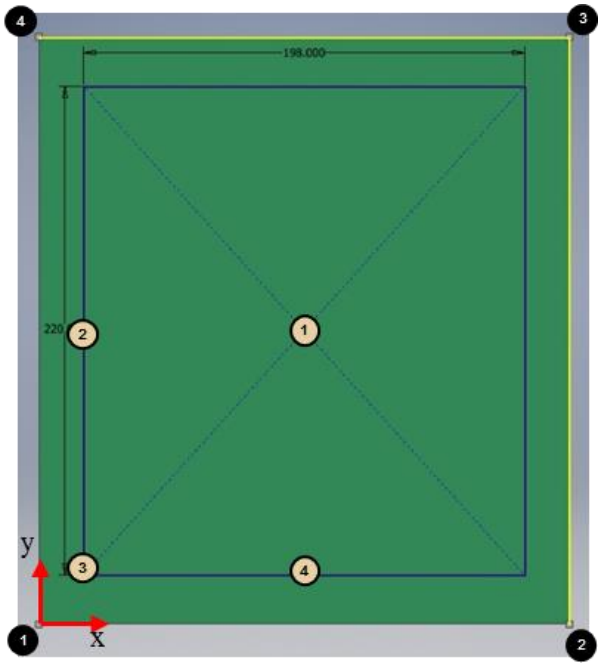

Figure 7-4: Experiment points in the field area

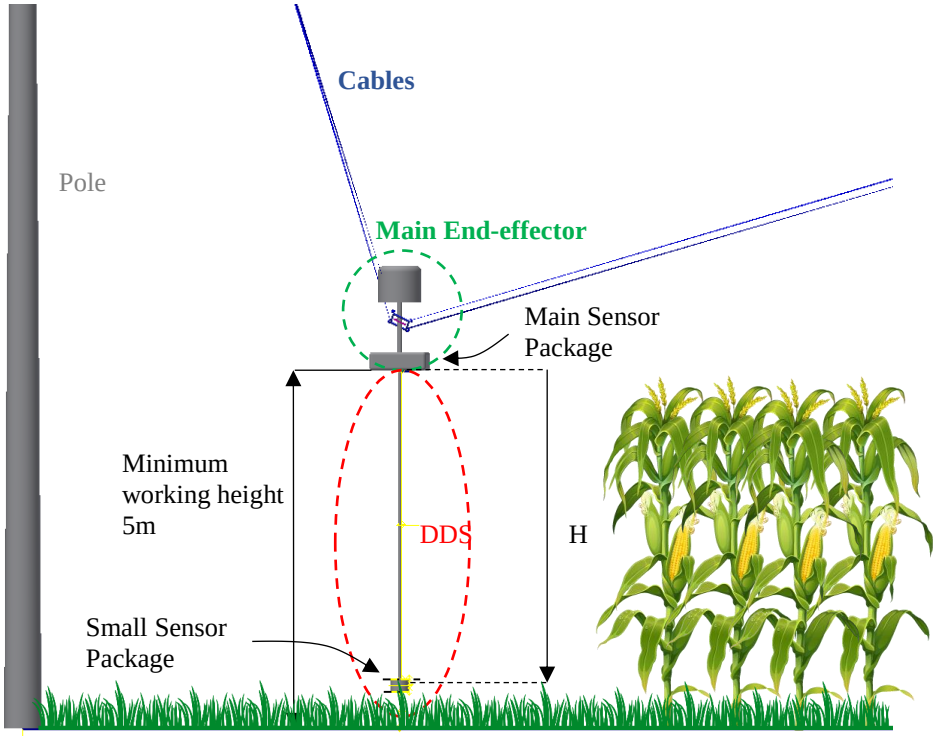

Figure 7-5: side view of DDS in the field

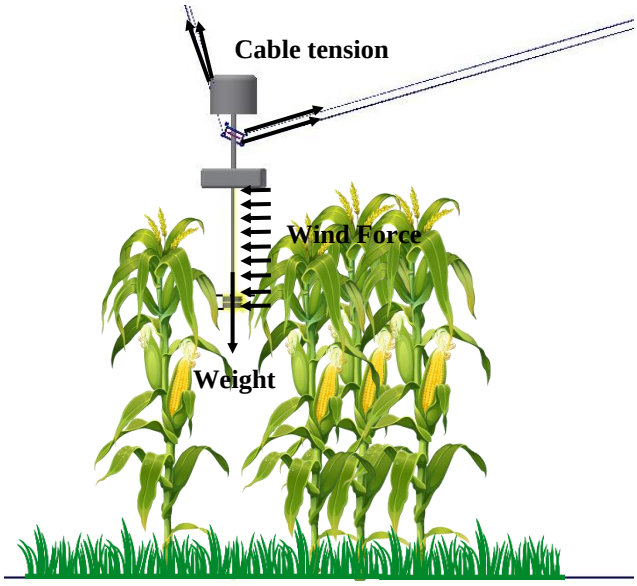

Figure 7-6: Free body diagram of DDS

Figure 7-7 shows the result of the maximum vibration amplitude of the small sensor package at the four critical positions at the field and the different lengths of the connection rod. The results indicate that the maximum vibration amplitude of the small end-effector at point 3 is higher than other points. In the worst case, the vibration amplitude at this point (the corner of the field) can reach 3.1 m, where the connecting rod is 5m, or the small sensor package is in the lowest position. Figure 7-8 shows the velocity profile of the small sensor package at this point when the small sensor package is 5 m inside the canopy.

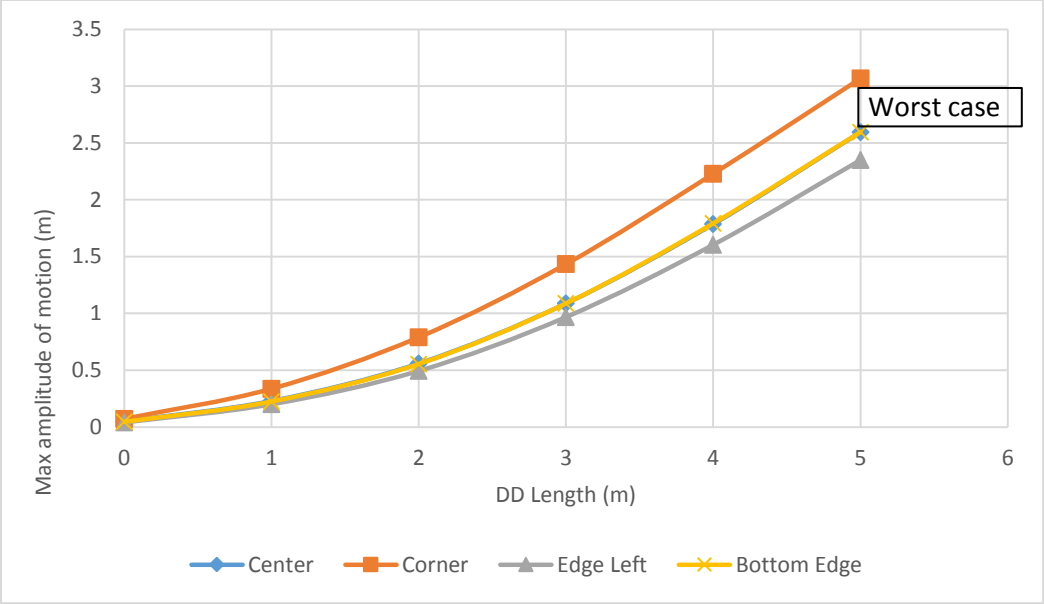

Figure 7-7: The result of simulation for the full-size DDS in four critical positions

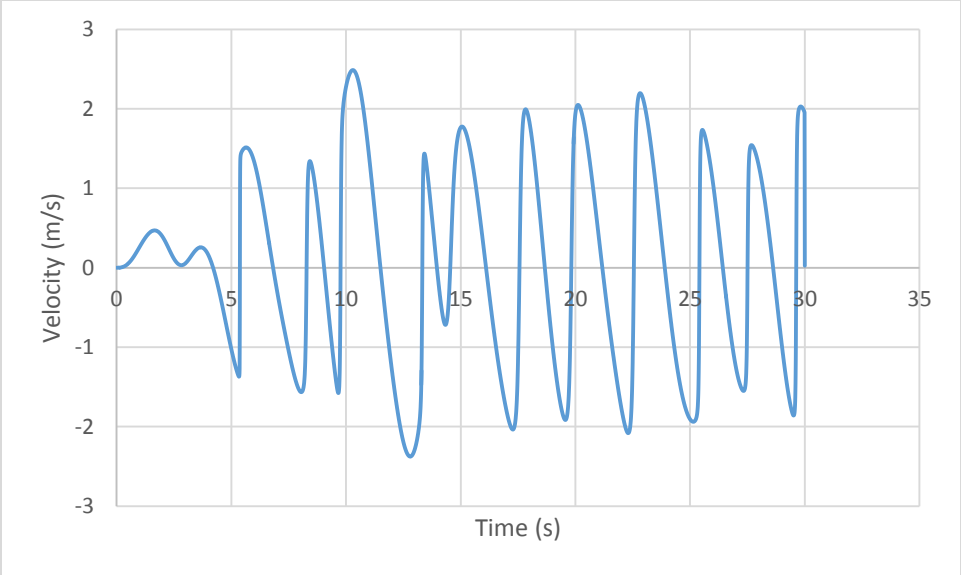

Figure 7-8: Velocity of the small end-effector in the corner with 5m drop-down arm

7.2 Results and discussion

This result shows that the vibration amplitude of the small sensor package is higher than the desired positioning accuracy of the sensor package (Table 2-1). Therefore, the cameras would not receive accurate data from the target plant. The high intensity of vibration not only troubles the operation of the DDS but also hinders the operation of the 4CDPM and the positioning of the

main end-effector. The obtained results in Chapter 3 for the maximum allowable vibration speed in the sensor package can be used here for better evaluation of the feasibility of the full-size DDS.

The results obtained in Chapter 3 state that the maximum allowable horizontal vibration speed of the end-effector must not exceed 5.36 mm/min when the sensor package is located at 50cm above the ground. However, the result of the DDS simulation shows that the maximum speed of the small end-effector is 2.48 m/s (or 148800 mm/min). In this study, for simplifying the simulation, the cables were assumed non-flexible, and wind force was only applied on the small sensor package and connecting rod. In reality, the flexible cables experience catenary due to their weight and vibrate when wind speed is significant. The vibration of the cables induces additional oscillations to the main sensor package, which exacerbates the stability of the end-effector. Therefore, the current DDS is considered not feasible to drop an additional sensor package into the canopy according to the results in this section.

7.3 Conclusion

In this chapter, first, a computer simulation was performed to study the effect of disturbances on the operation of the DDS. Next, the feasibility of using the DDS in the 4CDPM was determined by analyzing the sensitivity of the system to the different inputs. Results show that lowering a supplementary system for scanning low-level crops in the current 4CDPM causes several instability problems both to the main and small sensor package. Therefore, an additional stabilization system needs to be added to the current DDS to make it feasible for reliable operation in the field in different weather conditions.

In the next chapter, a small prototype of a drop-down system is built, which can be used in future research. A concept of the stabilization system is proposed in Chapter 9, which can be used in future designs.

Chapter 8 : Small scale prototype of DDS

As discussed in the previous chapters, the DDS descends an additional sensor package into the canopy where the main sensor package is not able to perform sensing or take images. The purpose of this chapter is to provide a platform for testing the stabilization system of the DDS in future research. In this chapter, first, the design specifications of the DDS are discussed, and solutions for possible problems are addressed. Next, a 12th scale prototype of the DDS is built according to the design constraints. Finally, the advantages and drawbacks of the system are discussed.

8.1 Design specifications

The maximum weight of the small sensor package in the full-scale DDS is 10 kg, and the dropping height is at most 5m. Therefore, by dividing these two values by 12, the scaled weight and lowering height of the 12^{th}-scale system are 830g and 42cm respectively.

The power consumption of components is one of the important factors in designing a 4CDPM because this system is using batteries as the main power supply. Electronic parts have to be in the sleep mode or be turned off when they are not being used. Therefore, the DDS, which is an additional system to the 4CDPM, must not influence the operation of the main sensor package by consuming additional energy. Hence, the electrical components of the DDS have to work with minimum power consumption and be switched off while not working.

8.2 Parts and assembly

A system of a DC motor, encoder, and drum can be used to raise or descend the small sensor package in the DDS. DC or AC motors convert electrical energy into mechanical energy such as rotation. When the motor is not powered, a small amount of torque on the output shaft can rotate the shaft and change its angular position. Therefore, the motor must be continuously

powered to keep the output shaft in the desired position. As mentioned above, the motor should not use any power while it is not being used for lifting or dropping the end-effector. One of the techniques for achieving this goal is to use a worm drive gearbox.

8.2.1 Gearbox design

A worm drive is a gear arrangement in which a worm (which is a gear in the form of a screw) meshes with a worm gear. Like other gear arrangements, a worm drive can reduce rotational speed or transmit higher torque, which is beneficial in the DDS. Unlike ordinary gear trains, the direction of transmission (input shaft vs. output shaft) is not reversible when using large reduction ratios, due to the greater friction involved between the worm and worm gear, when usually a single start (one spiral) worm is used. This can be an advantage when it is desired to eliminate any possibility of the output driving the input. Worm gear configurations in which the gear cannot drive the worm are called self-locking. Therefore, the motor does not need to be used to hold the weight of the small sensor package while it is scanning the plants at a specific height or is maintained in the sleep mode near the main sensor package. A 30:1 ratio worm-drive gearbox (Figure 8-1) is used to self-lock the system in the sleep mode.

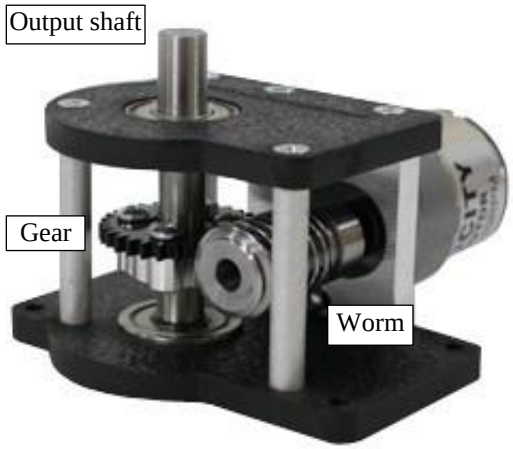

Figure 8-1: Worm gear box

8.2.2 Motor design

To select a suitable motor, it is necessary to know the required torque for raising and dropping the weight. As mentioned above, the maximum weight of the small sensor package was calculated to be 830g. A 3D printed drum with 21mm outside diameter (Figure 8-2), is used and a safety factor of 2.25 is considered to prevent causing the motor to stall or consume high current. The required torque can be found from the following relation.

$$\text{Required torque} = SF \times \frac{D}{2} Mg = 2.25 \times \frac{21}{2} \times 0.83 \times 9.81 = 196 \text{ mN.m} \quad (8\text{-}1)$$

where SF is the safety factor, D is the drum diameter, M is the weight of the small sensor package, and g is gravity. Therefore, in this system, a 12 V DC motor with a maximum speed of 1100 rpm and maximum torque of 196.133 mN.m is used to lift the sensor package (Figure 8-3).

Figure 8-2: 3D printed drum

Figure 8-3: DC motor

A E6B2-CWZ3E Yumo rotary encoder with 1024 pulses per revolution is used to convert the angular position or motion of the gearbox output shaft to an analog code for better controlling the position of the motor [77].

Figure 8-4: The rotary encoder [77]

To model the small sensor package, an 830g mass is connected to the cable using an eye screw. The cable is coiled around the drum, which is mounted on the output shaft of the worm gearbox. The DDS driving system is controlled by an Arduino Mega 2560 microcontroller, and Arduino software is used to program the microcontroller. A Bluetooth modem makes the connection between the computer and the controller. The controller is programmed to drive the motor with smooth motion without quick release or pulling the cable. Small start and stop acceleration maintains the stability of the system and avoids extra torque on the motor.

The final assembly is shown in Figure 8-5a. A plate with a circular pattern of holes is connected on top of the battery package where the extra weights can be mounted to balance the COM. Figure 8-5b shows a gimbal system that is used for connecting the cables to the end-effector. The motorized driving system (Figure 8-5c) uses the self-lock worm gearbox to prevent the batteries from draining power when the small sensor package is in position for scanning the plants. The battery package provides enough power for running the microcontroller and the driving the winch system.

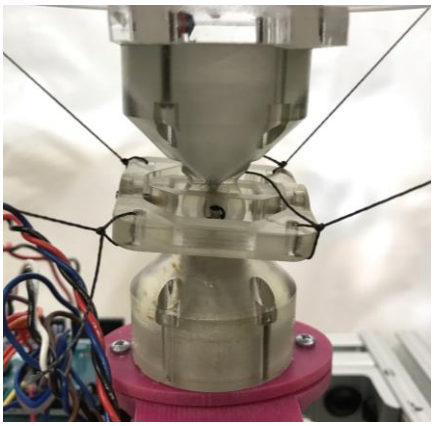

(b)

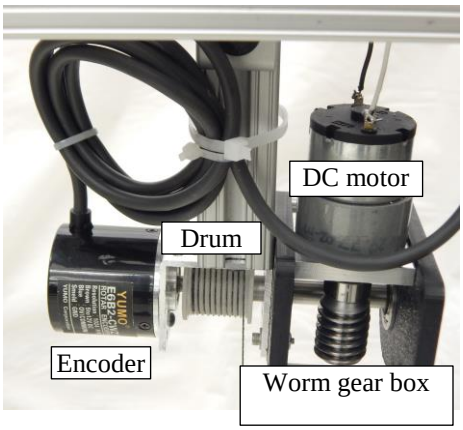

(c)

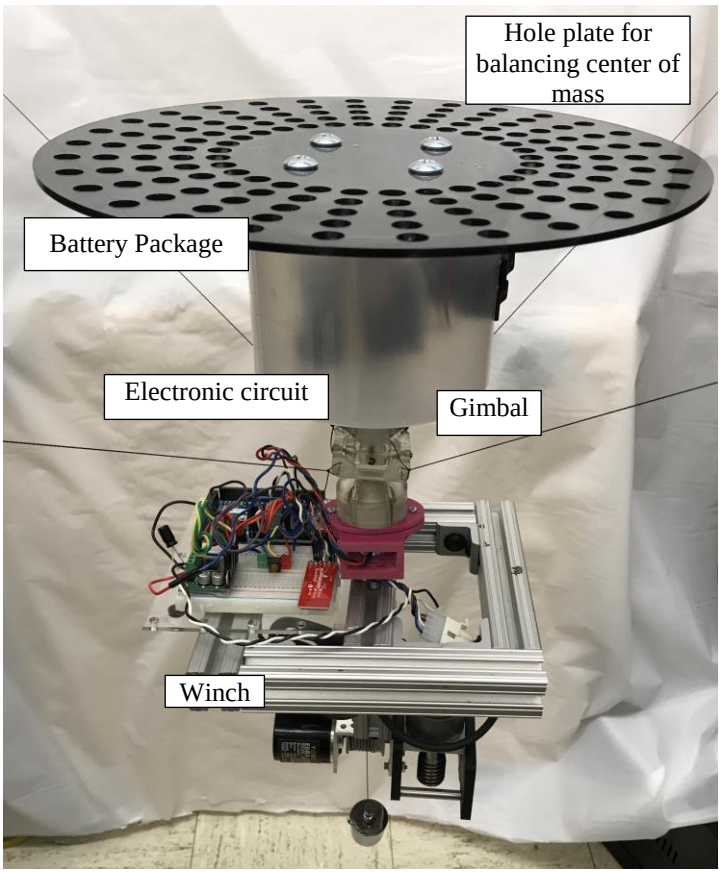

(a)

Figure 8-5: a) DDS model assembly; b) Gimbal system; c) Drive system

8.3 Functionality Test

The driving system, data communication, and the controller are tested in this section to prove their proper functionality.

8.3.1 Test method

First, the functionality of the controller is tested by applying different input commands to the controller via a computer interface and measuring the output voltage of each pin on the Arduino. The computer is then located to the further location to test the proper function of the Bluetooth modem at far distances. The functionality of the winch system is tested by mounting

several weights ranging from 50g to 1000g. A camera is also connected to the dropping weight for monitoring the weight vibrations while being lowered or raised.

8.3.2 Test results

The result of the controller test shows that all of the pins responded correctly to the input user commands. The communication modem works great when the computer is located within 10 m away from the controller but does not work accurately at longer distances from 10 to 18 m. The winch system is capable of raising weights under 850 g without stalling; however, for weights greater than 850g, it stalls in the upward motion. The captured video of the camera shows a significant amount of pendulum when the weight is traveling upward and downward. This pendulum vibration is expected to be significantly larger in an outdoor condition where the wind drag is applied to the system. The main reasons for this pendulum vibration are the flexibility of the cable and the lack of any constraint restricting the pendulum movement of the weight.

8.4 Conclusion

In this chapter, a proof of concept prototype for the DDS was designed, built, and tested. The purpose of this chapter is to provide a platform for testing the stabilization system of the DDS in future research. This portable prototype is a convenient system, which is able to meet the desired specifications of the full-size system in 12^{th}-scale. In this chapter, first, each part was designed according to the design specifications of the DDS. Next, parts were assembled, and the functionally of subassemblies were tested. The results of the tests showed an adequate performance of the operation of the system, meeting all the design features. However, the large pendulum of the suspended weight was the main problem, which needs to be addressed in future research.

Chapter 9 : Discussion and Conclusion

This thesis presents the design and testing of two subsystems for the end-effector of a 4CDPM. In Part I, a center of mass balancing system was presented to minimize the vibration and enhance the stability, accuracy, and quality of acquired data from the instruments in the sensor package.

The sensor package is one of the most important parts of the end-effector of a 4CDPM, which consists of a variety of sensors and electronic devices with different sizes and weights. Researchers sometimes need to add, remove, or swap sensors in the sensor package to reach their sensing objectives. Any changes in the position of components inside the sensor package can change the COM of the whole end-effector resulting in instability during movement. To prevent this, an easy to use passive system was designed, which enables researchers to adjust the COM simply. The described system provides this ability using two circular plates with a pattern of holes for weight attachment and a rod for mounting the circular plates in different heights. A combination of weight arrangements with plate movement along the vertical rod provides enough resolution for COM adjustment. Researchers can use the proposed COM finder apparatus and automated computer program to locate the weights in the best position.

Moreover, in this research two series of experiments were performed to determine the influence of the COM offset on dynamic equilibrium of the end-effector and prove the CMBS functionality. The experimental results showed that the COM position plays a major role in the stability of the 4CDMR end-effector. The results proved that because of using a gimbal system, the COM must be on the axis of symmetry of the end-effector; otherwise, an external moment is applied on the gimbal, causing the end-effector to tilt. It was observed that a COM under the gimbal

pivot point could cause a severe pendulum movement with high frequency and large amplitude of motion vibration. In conclusion, the CMBS easily moves the COM position to the axis of symmetry or the cable's connection point to reduce the pendulum effect and vibrations.

In Part II, the feasibility of a dolly subsystem was determined. This system can noninvasively lowers a phenotyping sensor package into the canopy at the leaf level. This system also can be used for studying soil and vegetation at various heights in the canopy level.

A dynamic simulation of the DDS was performed in the CAD software, and the results were compared to a physical experiment to validate the accuracy of the software's result. The results showed that the software is able to simulate the physical system properly. Therefore, the software was used alone for further analysis without producing a physical prototype.

The full-size model of the DDS was analyzed in a CAD software according to different conditions such as different lengths of the lowering arm, and environmental disturbances. In addition, a sensitivity analysis of the DDS was performed, and the preliminary feasibility of the DDS concept was determined. This result showed that the vibration amplitude of the small sensor package is higher than the desired positioning accuracy of the sensor package in Table 2-1, making the system impossible to use. The high intensity of the vibration speed and amplitude not only troubles the operation of the DDS but also hinders the operation of the 4CDPM and the positioning of the main end-effector.

Finally, in Chapter 8, a 12^{th}-scale platform of the DDS was designed, built, and tested. The purpose of building this platform was to facilitate the future studies on the DDS stabilization system. Each part was designed according to the design specifications of the DDS. Parts were assembled, and the functionality of subassemblies were tested. The results of the tests

demonstrated the operation of the system, met all design features. However, the high pendulum movement of the suspended weight is a problem, which needs to be addressed in future research.

9.1 Future Works

The total motion blur of 1% was used for calculating the dynamic stability of the end-effector (Chapter 3). This number needs to be altered in a way to be more scientifically accepted. Therefore, more research needs to be done to provide more reliable information about the maximum allowable motion blur that does not change the radiometric results significantly.

The COM finder apparatus and computer program in Chapter 4 need to be designed and tested in future research. They can be used for facilitating the positioning of the weights in the CMBS.

The feasibility of using a sub system for low-level scanning of crops known as the drop-down system (DDS) was determined (Chapter 7). A 12^{th}-scale proof of concept for the DDS was designed and built (Chapter 8). It was concluded that a high pendulum effect and the vibration of the small package are important factors, which make the system impossible to use for scanning crops.

Future work will need to design an active stabilization system that can be used to improve the positioning and reliability of the DDS. In addition, the operational speed of dropping and raising the sensor package, and the type of sensors in the small sensor package needs to be known for better specification of the stabilization design.

In this chapter, the concept of an active stabilization system is proposed that can be used for damping the vibrations of the DDS end-effector during operation in the field.

9.2 Stabilization System Conceptualization

A quadcopter also called a quadrotor helicopter, drone or quadrotor [78] is a multi rotor helicopter that is lifted and propelled by four rotors. In the past few years, flying drones have become more popular and much more affordable leading to new uses of drones for research or business. In this research, however, an inverted drone is proposed to stabilize the DDS (Figure 9-1). In this system, the propeller's thrust is upward unlike the usual drone, which makes a downward thrust to fly. The inverted copter should be connected to the small sensor package in the DDS as shown in Figure 9-2. This system provides only stabilization and does not support the weight of the sensor package. The motorized drum and cable discussed in the last chapter will provide enough support for the weight of the DDS's sensor package.

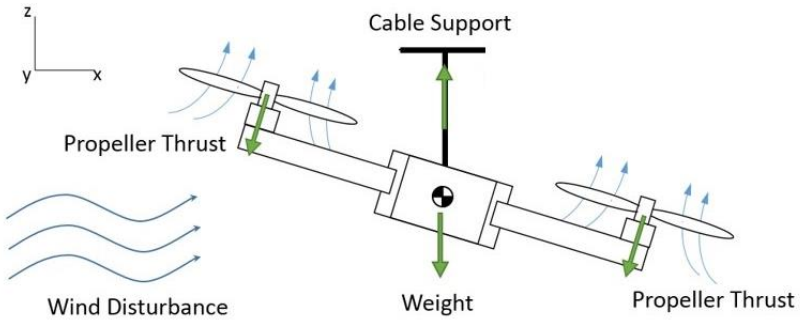

Figure 9-1: Stabilization System Model

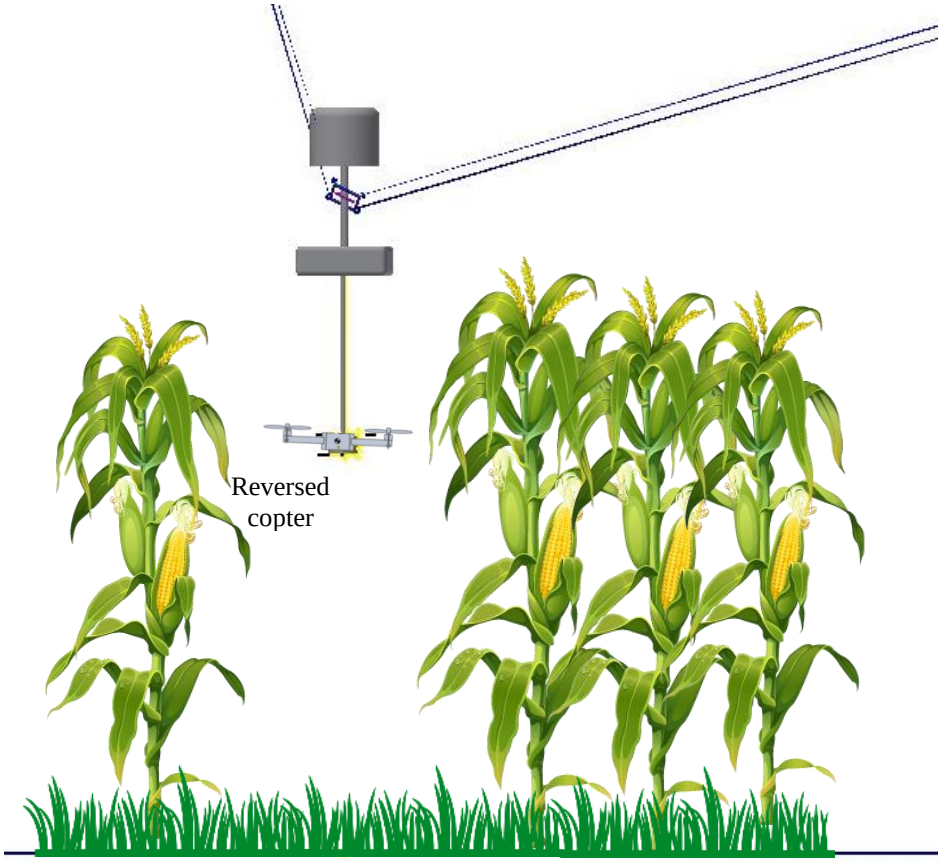

Figure 9-2: Using inverted copter in DDS

The quadcopter stabilization system is a low-cost method, compared to other active stabilization methods since the control theory has been thoroughly developed, and manufactured kits are available for development. Also, it has an accurate positioning system with high repeatability. Therefore, the inverted quadcopter can be used as a potential system for stabilizing the sensor package of the DDS. It is necessary to mention that this system only can be used when the small sensor package is lowered into the area between each canopy plot; otherwise, it would cut the leaves and cause critical damage to the plant.

References

[1] M. V. Boggess *et al.*, "The need for agriculture phenotyping: 'Moving from genotype to phenotype,'" *J. Proteomics*, vol. 93, pp. 20–39, Nov. 2013.

[2] "International Plant Phenotyping Network." [Online]. Available: https://www.plant-phenotyping.org/index.php?index=386. [Accessed: 29-Jun-2017].

[3] L. Li, Q. Zhang, and D. Huang, "A Review of Imaging Techniques for Plant Phenotyping," *Sensors*, vol. 14, no. 11, pp. 20078–20111, Oct. 2014.

[4] N. J. J. Bréda, "Ground-based measurements of leaf area index: a review of methods, instruments and current controversies," *J. Exp. Bot.*, vol. 54, no. 392, pp. 2403–2417, Nov. 2003.

[5] M. Jansen *et al.*, "Simultaneous phenotyping of leaf growth and chlorophyll fluorescence via GROWSCREEN FLUORO allows detection of stress tolerance in Arabidopsis thaliana and other rosette plants," *Funct. Plant Biol.*, vol. 36, no. 11, pp. 902–914, Nov. 2009.

[6] "Genetic Variation of Plant Height and Stem Diameter Traits in Maize (Zea mays L.) under Drought Stress at Different Growth Stages," *ResearchGate*. [Online]. Available: https://www.researchgate.net/publication/270275440_Genetic_Variation_of_Plant_Height_and_Stem_Diameter_Traits_in_Maize_Zea_mays_L_under_Drought_Stress_at_Different_Growth_Stages. [Accessed: 29-Jun-2017].

[7] A. Bucksch *et al.*, "Image-Based High-Throughput Field Phenotyping of Crop Roots," *Plant Physiol.*, vol. 166, no. 2, pp. 470–486, Oct. 2014.

[8] S. V. Ollinger, "Sources of variability in canopy reflectance and the convergent properties of plants," *New Phytol.*, vol. 189, no. 2, pp. 375–394, Jan. 2011.

[9] "Quantitative trait loci associated with tipburn, heat stress-induced physiological disorders, and maturity traits in crisphead lettuce - ProQuest." [Online]. Available: http://search.proquest.com/openview/620b40b9923ab48d2ae4b447571b962a/1?pq-origsite=gscholar&cbl=54040. [Accessed: 29-Jun-2017].

[10] B.-C. Dong, G.-L. Yu, W. Guo, M.-X. Zhang, M. Dong, and F.-H. Yu, "How internode length, position and presence of leaves affect survival and growth of Alternanthera philoxeroides after fragmentation?," *Evol. Ecol.*, vol. 24, no. 6, pp. 1447–1461, Nov. 2010.

[11] D. Kendal, C. E. Hauser, G. E. Garrard, S. Jellinek, K. M. Giljohann, and J. L. Moore, "Quantifying Plant Colour and Colour Difference as Perceived by Humans Using Digital Images," *PLOS ONE*, vol. 8, no. 8, p. e72296, Aug. 2013.

[12] A. Berg, S. Kjelvik, and F. E. Wielgolaski, "Measurement of Leaf Areas and Leaf Angles of Plants at Hardangervidda, Norway," in *Fennoscandian Tundra Ecosystems*, F. E. Wielgolaski, Ed. Springer Berlin Heidelberg, 1975, pp. 103–110.

[13] J. C. O'Toole, R. T. Cruz, and T. N. Singh, "Leaf rolling and transpiration," *Plant Sci. Lett.*, vol. 16, no. 1, pp. 111–114, Sep. 1979.

[14] S. Nagelmüller, N. Kirchgessner, S. Yates, M. Hiltpold, and A. Walter, "Leaf Length Tracker: a novel approach to analyse leaf elongation close to the thermal limit of growth in the field," *J. Exp. Bot.*, vol. 67, no. 6, pp. 1897–1906, Apr. 2016.

[15] T. Tanabata, T. Shibaya, K. Hori, K. Ebana, and M. Yano, "SmartGrain: High-Throughput Phenotyping Software for Measuring Seed Shape through Image Analysis1[C][W][OA]," *Plant Physiol.*, vol. 160, no. 4, pp. 1871–1880, Dec. 2012.
[16] Karol Paulette Constantino, Elisha Jeremy Gonzales, Lordd Michael Lazaro, Ellen Chelsea Serrano, and Briane Paul Samson, "Plant Height Measurement and Tiller Segmentation of Rice Crops Using Image Processing," *DLSU Res. Congr.*, vol. 3, 2015.
[17] B. Chacón, R. Ballester, V. Birlanga, A.-G. Rolland-Lagan, and J. M. Pérez-Pérez, "A Quantitative Framework for Flower Phenotyping in Cultivated Carnation (Dianthus caryophyllus L.)," *PLOS ONE*, vol. 8, no. 12, p. e82165, Dec. 2013.
[18] A. D. Aquila, "Digital imaging information technology applied to seed germination testing. A review," *Agron. Sustain. Dev.*, vol. 29, no. 1, pp. 213–221, Mar. 2009.
[19] T. Lillesand, R. W. Kiefer, and J. Chipman, *Remote Sensing and Image Interpretation*. John Wiley & Sons, 2014.
[20] C. Atzberger, "Advances in Remote Sensing of Agriculture: Context Description, Existing Operational Monitoring Systems and Major Information Needs," *Remote Sens.*, vol. 5, no. 2, pp. 949–981, 22 2013.
[21] "HYPERSPECTRAL SENSORS| IEEE | Geoscience & Remote Sensing Society," *GRSS | IEEE | Geoscience & Remote Sensing Society*. .
[22] J. Xue and B. Su, "Significant Remote Sensing Vegetation Indices: A Review of Developments and Applications," *Journal of Sensors*, 2017. [Online]. Available: https://www.hindawi.com/journals/js/2017/1353691/. [Accessed: 29-Jun-2017].
[23] L. Li, C. Solana, F. Canters, J. C.-W. Chan, and M. Kervyn, "Impact of Environmental Factors on the Spectral Characteristics of Lava Surfaces: Field Spectrometry of Basaltic Lava Flows on Tenerife, Canary Islands, Spain," *Remote Sens.*, vol. 7, no. 12, pp. 16986–17012, Dec. 2015.
[24] D. Rundquist, A. Gitelson, B. Leavitt, A. Zygielbaum, R. Perk, and G. Keydan, "Elements of an Integrated Phenotyping System for Monitoring Crop Status at Canopy Level," *Agronomy*, vol. 4, no. 1, pp. 108–123, 17 2014.
[25] E. J. Milton, M. E. Schaepman, K. Anderson, M. Kneubühler, and N. Fox, "Progress in field spectroscopy," *Remote Sens. Environ.*, vol. 113, Supplement 1, p. S109, Sep. 2009.
[26] K. P. Price, V. C. Varner, E. A. Martinko, D. C. Rundquist, and J. S. Peake, "Influences of land management and weather on plant biophysical and hyper-spectral response patterns of tallgrass prairies in northeastern Kansas," in *Proceedings, Pecora 12 Symposium, August 24-26, 1993, Sioux Falls, South Dakota*, 1993, pp. 441–450.
[27] D. Rundquist, R. Perk, B. Leavitt, G. Keydan, and A. Gitelson, "Collecting spectral data over cropland vegetation using machine-positioning versus hand-positioning of the sensor," *Comput. Electron. Agric.*, vol. 43, no. 2, pp. 173–178, May 2004.
[28] "MISR validation activities and results." [Online]. Available: https://misr.jpl.nasa.gov/Mission/valwork/mivalres.html. [Accessed: 11-Jul-2017].
[29] S. Sankaran *et al.*, "Low-altitude, high-resolution aerial imaging systems for row and field crop phenotyping: A review," *Eur. J. Agron.*, vol. 70, pp. 112–123, Oct. 2015.
[30] M. Zaman-Allah *et al.*, "Unmanned aerial platform-based multi-spectral imaging for field phenotyping of maize," *Plant Methods*, vol. 11, p. 35, Jun. 2015.
[31] C. A. Rokhmana, "The Potential of UAV-based Remote Sensing for Supporting Precision Agriculture in Indonesia," *Procedia Environ. Sci.*, vol. 24, pp. 245–253, Jan. 2015.

[32] “The Advantages Of Drone Remote Sensing For Agricultural Crops| Aerial Surveying & Mapping using Drones,” *SenSat | Aerial Surveying & Mapping using Drones*. [Online]. Available: https://www.sensat.co.uk/single-post/2015/07/25/The-Advantages-Of-Drone-Remote-Sensing-For-Agricultural-Crops. [Accessed: 11-Jul-2017].
[33] N. Virlet, K. Sabermanesh, P. Sadeghi-Tehran, and M. J. Hawkesford, “Field Scanalyzer: An automated robotic field phenotyping platform for detailed crop monitoring,” *Funct. Plant Biol.*, vol. 44, no. 1, pp. 143–153, 25 2017.
[34] P. Sadeghi-Tehran, K. Sabermanesh, N. Virlet, and M. J. Hawkesford, “Automated Method to Determine Two Critical Growth Stages of Wheat: Heading and Flowering,” *Front. Plant Sci.*, vol. 8, 2017.
[35] L. Zhang, X. Sun, T. Wu, and H. Zhang, “An Analysis of Shadow Effects on Spectral Vegetation Indexes Using a Ground-Based Imaging Spectrometer,” *IEEE Geosci. Remote Sens. Lett.*, vol. 12, no. 11, pp. 2188–2192, Nov. 2015.
[36] “Characteristics of shadow and removal of its effects for remote sensing imagery,” *ResearchGate*. [Online]. Available: https://www.researchgate.net/publication/224116810_Characteristics_of_shadow_and_removal_of_its_effects_for_remote_sensing_imagery. [Accessed: 11-Jul-2017].
[37] A. Shahtahmassebi, N. Yang, K. Wang, N. Moore, and Z. Shen, “Review of shadow detection and de-shadowing methods in remote sensing,” *Chin. Geogr. Sci.*, vol. 23, no. 4, pp. 403–420, Aug. 2013.
[38] A. Pott *et al.*, “Cable-driven parallel robots for industrial applications: The IPAnema system family,” in *IEEE ISR 2013*, 2013, pp. 1–6.
[39] “Serial manipulator,” *Wikipedia*. 24-Feb-2016.
[40] “Robot end effector,” *Wikipedia*. 27-Jun-2017.
[41] “Parallel manipulator,” *Wikipedia*. 23-Oct-2016.
[42] “Cable robots,” *Wikipedia*. 24-Jun-2017.
[43] “Optimal Design of Cable-Driven Parallel Robots for Large Industrial Structures,” *ResearchGate*. [Online]. Available: https://www.researchgate.net/publication/263714205_Optimal_Design_of_Cable-Driven_Parallel_Robots_for_Large_Industrial_Structures. [Accessed: 29-Jun-2017].
[44] N. Fabjan, “spidercam - home,” *Spidercam*. [Online]. Available: http://www.spidercam.tv/. [Accessed: 29-Jun-2017].
[45] N. G. Dagalakis, J. S. Albus, B. Wang, J. Unger, and J. W. Lee, “Stiffness Study of a Parallel Link Robot Crane for Shipbuilding Applications,” in *NIST*, 1988.
[46] J. Albus, R. Bostelman, and N. Dagalakis, “The NIST robocrane,” *J. Robot. Syst.*, vol. 10, no. 5, pp. 709–724, Jul. 1993.
[47] “On Design of a Redundant Wire-Driven Parallel Robot WARP Manipulator.” [Online]. Available: /paper/On-Design-of-a-Redundant-Wire-Driven-Parallel-Robo-Maeda-Tadokoro/41d8ce2f1ad2868c8b121edde3690f4923a7cee9. [Accessed: 29-Jun-2017].
[48] S. Tadokoro, R. Verhoeven, M. Hiller, and T. Takamori, “A portable parallel manipulator for search and rescue at large-scale urban earthquakes and an identification algorithm for the installation in unstructured environments,” in *Proceedings 1999 IEEE/RSJ International Conference on Intelligent Robots and Systems. Human and Environment Friendly Robots with High Intelligence and Emotional Quotients (Cat. No.99CH36289)*, 1999, vol. 2, pp. 1222–1227 vol.2.

[49] “Design of a Parallel Wire-Driven Manipulator for Wind Tunnels - Semantic Scholar.” [Online]. Available: /paper/Design-of-a-Parallel-Wire-Driven-Manipulator-for-W-Gosselin-LAFOURCADE/411a107111e1aac4ff34f9415f3e35ce0b614b98. [Accessed: 30-Jun-2017].

[50] “Analysis of the Workspace of Tendon-based Stewart Platforms,” *ResearchGate*. [Online]. Available: https://www.researchgate.net/publication/29800003_Analysis_of_the_Workspace_of_Tendon-based_Stewart_Platforms. [Accessed: 30-Jun-2017].

[51] M. Hiller, S. Fang, S. Mielczarek, R. Verhoeven, and D. Franitza, “Design, analysis and realization of tendon-based parallel manipulators,” *Mech. Mach. Theory*, vol. 40, no. 4, pp. 429–445, Apr. 2005.

[52] J. Huang, T. Pretz, and Z. Bian, “Modeling and motion control simulation of tendon based parallel manipulator translation mechanism for sensor based high value waste processing,” *J. Cent. South Univ. Technol.*, vol. 18, no. 6, pp. 1953–1961, Dec. 2011.

[53] D. Surdilovic and R. Bernhardt, “STRING-MAN: a new wire robot for gait rehabilitation,” in *2004 IEEE International Conference on Robotics and Automation, 2004. Proceedings. ICRA ’04*, 2004, vol. 2, p. 2031–2036 Vol.2.

[54] D. Surdilovic, J. Zhang, and R. Bernhardt, “STRING-MAN: Wire-robot technology for safe, flexible and human-friendly gait rehabilitation,” in *2007 IEEE 10th International Conference on Rehabilitation Robotics*, 2007, pp. 446–453.

[55] M. J.-D. Otis, S. Comtois, D. Laurendeau, and C. Gosselin, “Human Safety Algorithms for a Parallel Cable-Driven Haptic Interface,” in *Brain, Body and Machine*, Springer, Berlin, Heidelberg, 2010, pp. 187–200.

[56] M. J. D. Otis *et al.*, “Determination and Management of Cable Interferences Between Two 6-DOF Foot Platforms in a Cable-Driven Locomotion Interface,” *IEEE Trans. Syst. Man Cybern. - Part Syst. Hum.*, vol. 39, no. 3, pp. 528–544, May 2009.

[57] Jörg-Dieter Walz, “Cable-driven parallel robots - Fraunhofer IPA,” *Fraunhofer Institute for Manufacturing Engineering and Automation IPA*. [Online]. Available: http://www.ipa.fraunhofer.de/en/press/2015-09-09_Cable-driven-parallel-robots.html. [Accessed: 30-Jun-2017].

[58] R. Nan *et al.*, “The five-hundred-meter aperture spherical radio telescope (FAST) project,” *Int. J. Mod. Phys. D*, vol. 20, no. 06, pp. 989–1024, 2011.

[59] R. Nan, “Five hundred meter aperture spherical radio telescope (FAST),” *Sci. China Ser. G*, vol. 49, no. 2, pp. 129–148, Apr. 2006.

[60] Z.-F. Shao, X. Tang, L.-P. Wang, and X. Chen, “Dynamic modeling and wind vibration control of the feed support system in FAST,” *Nonlinear Dyn.*, vol. 67, no. 2, pp. 965–985, Jan. 2012.

[61] R. Yao, X. Tang, J. Wang, and P. Huang, “Dimensional Optimization Design of the Four-Cable-Driven Parallel Manipulator in FAST,” *IEEEASME Trans. Mechatron.*, vol. 15, no. 6, pp. 932–941, Dec. 2010.

[62] N. Kirchgessner *et al.*, “The ETH field phenotyping platform FIP: a cable-suspended multi-sensor system,” *Funct. Plant Biol.*, vol. 44, no. 1, pp. 154–168, 25 2017.

[63] N. Kirchgessner, “Field imaging platform (FIP) - an automated system for plant phenotyping in the field,” in *Bornimer agrartechnische Berichte*, 2015, vol. 88, pp. 74–81.

[64] “Eye in the sky to monitor crops.” [Online]. Available: https://www.ethz.ch/en/news-and-events/eth-news/news/2016/06/eye-in-the-sky-to-monitor-crops.html. [Accessed: 10-Jul-2017].

[65] Brenda Ortiz and Joey N. Shaw, “Basics of Crop Sensing.”
[66] “Motion blur,” *Wikipedia*. 14-May-2017.
[67] H. Photonics, “Hyperspec INSPECTOR.” [Online]. Available: http://www.headwallphotonics.com/spectral-imaging/hyperspectral/hyperspec-inspector. [Accessed: 10-Jul-2017].
[68] H. Photonics, “Hyperspec INSPECTOR.” [Online]. Available: http://www.headwallphotonics.com/spectral-imaging/hyperspectral/hyperspec-inspector. [Accessed: 11-Jul-2017].
[69] “HR4000 (Custom),” *Ocean Optics*. [Online]. Available: https://oceanoptics.com/product/hr4000-custom/. [Accessed: 11-Jul-2017].
[70] “Spectral Evolution, Inc. --- spectrometer products for remote sensing, mining and general photonics.” [Online]. Available: http://www.spectralevolution.com/spectrometers.html. [Accessed: 11-Jul-2017].
[71] “FLIR Advanced Thermal Solutions: FLIR A655sc Infrared Camera for Research & Science.” [Online]. Available: http://www.flir.com/science/display/?id=46802. [Accessed: 11-Jul-2017].
[72] “Precision Agriculture: Remote Sensing and Ground Truthing | University of Missouri Extension.” [Online]. Available: http://extension.missouri.edu/p/eq453. [Accessed: 19-Jun-2017].
[73] “Application of remote sensing methods in agriculture,” *ResearchGate*. [Online]. Available: https://www.researchgate.net/publication/290494859_Application_of_remote_sensing_methods_in_agriculture. [Accessed: 19-Jun-2017].
[74] Y. Ge, J. A. Thomasson, and R. Sui, “Remote sensing of soil properties in precision agriculture: A review,” *Front. Earth Sci.*, vol. 5, no. 3, pp. 229–238, Sep. 2011.
[75] J.-P. Ore, S. Elbaum, A. Burgin, and C. Detweiler, “Autonomous Aerial Water Sampling,” *J. Field Robot.*, vol. 32, no. 8, pp. 1095–1113, Dec. 2015.
[76] “Amazon patents delivery drone designs with adjustable arms and a winch,” *GeekWire*, 13-Jun-2017. [Online]. Available: https://www.geekwire.com/2017/amazon-patents-delivery-drone-designs-adjustable-arms-winch/. [Accessed: 30-Jun-2017].
[77] “Rotary Encoder - 1024 P/R (Quadrature) - COM-11102 - SparkFun Electronics.” [Online]. Available: https://www.sparkfun.com/products/11102. [Accessed: 17-Jul-2017].
[78] G. Hoffmann, D. G. Rajnarayan, S. L. Waslander, D. Dostal, J. S. Jang, and C. J. Tomlin, “The Stanford testbed of autonomous rotorcraft for multi agent control (STARMAC),” in *The 23rd Digital Avionics Systems Conference (IEEE Cat. No.04CH37576)*, 2004, vol. 2, p. 12.E.4-121-10 Vol.2.

Appendix 1

1.1 The complete result of vibration frequency and amplitude in the CMBS experiments

Table 9-1. Vibration experiment for balanced and unbalanced end-effector

			Pitch		Roll	
Point number	Moving direction	COM	Maximum Frequency (Hz)	Maximum Amplitude (degree)	Maximum Frequency (Hz)	Maximum Amplitude (degree)
1	High Front to Back	Balance	0.6	3.125	0.61	0.6875
		Unbalanced	1.83	10.125	1.81	2.18
	High Left to Right	Balance	0.573	0.5	0.611	3.125
		Unbalanced	1.82	2.93	1.831	13.98
	Low Front to Back	Balance	0.612	5.5	0.572	0.75
		Unbalanced	1.82	14.6	1.814	3.68
	Low Left to Right	Balance	0.573	0.687	0.613	4.06
		Unbalanced	1.832	11.375	1.834	19
2	High Front to Back	Balance	0.611	3.75	0.57	1.0625
		Unbalanced	1.83	9.875	1.83	6.43
	High Right to Left	Balance	0.704	0.3	0.539	4.1875
		Unbalanced	1.828	1.0625	1.831	7.81
	Low Front to Back	Balance	0.572	2.43	0.574	1.93
		Unbalanced	1.838	12.06	1.838	2.18
	Low Right to Left	Balance	0.61	1.5	1.14	2.25
		Unbalanced	1.834	3.25	1.838	9.25
3	High Back to Front	Balance	0.611	2.43	0.61	0.5
		Unbalanced	1.828	11.43	1.834	2.5

	High Right to Left	Balance	0.571	0.25	1.303	1.5
		Unbalanced	2.293	0.9375	1.824	4
	Low Back to Front	Balance	0.571	4.75	0.571	1.25
		Unbalanced	1.828	8.875	1.83	3.05
	Low Right to Left	Balance	0.57	0.625	0.505	2.125
		Unbalance	1.83	3.56	1.824	7.68
4	High Back to Front	Balance	0.571	2.6851	0.573	0.4375
		Unbalance	1.834	10.68	1.834	1.937
	High Left to Right	Balance	0.65	0.8125	0.656	0.875
		Unbalance	1.824	2.81	1.821	3.875
	Low Back to Front	Balance	0.609	3.0625	0.538	0.375
		Unbalance	1.821	6.5	1.831	1.375
	Low Left to Right	Balance	0.573	2.5	0.571	2.0625
		Unbalance	1.831	3.375	1.8315	3.68

Appendix 2

As a part of this research, the CMBS and DDS were designed, modeled, and tested. The CAD files and the computer programs for both system are available at

https://unl.box.com/s/x1wx850tncgqr1dvan6r248w98j4d0i9

This directory includes two folders for the CMBS and DDS. Each folder consists of several subfolders for different versions of the CMBS and DDS.